An Exact, Generalized Laplace Resonance in the HR 8799 Planetary System

Krzysztof Goździewski and Cezary Migaszewski
Faculty of Physics, Astronomy and Informatics, Nicolaus Copernicus Univ., Grudziądzka 5, Toruń, Poland; k.gozdziewski@umk.pl
Received 2020 August 22; revised 2020 September 13; accepted 2020 September 15; published 2020 October 20

Abstract

A system of four super-Jupiter planets around HR 8799 is the first multiplanet configuration discovered via the direct imaging technique. Despite over a decade of research, the system's architecture is still not fully resolved. The main difficulty comes from a still narrow observing window of ∼20 yr that covers small arcs of orbits with periods from roughly 50 to 500 yr. Soon after the discovery, it became clear that unconstrained best-fitting astrometric configurations self-disrupt rapidly due to strong mutual gravitational interactions between the companions of ≃10 Jupiter mass. Recently, we showed that the HR 8799 system may be long-term stable when locked in a generalized Laplace 8:4:2:1 mean-motion resonance (MMR) chain, and we constrained its orbits through the planetary migration. Here we qualitatively improve this approach by considering the MMR in terms of an exactly periodic configuration. This assumption enables us to construct for the first time the self-consistent *N*-body model of the long-term stable orbital architecture using only available astrometric positions of the planets relative to the star. We independently determine the planetary masses, which are consistent with thermodynamic evolution, and the parallax overlapping to 1σ with the most recent Gaia DR2 value. We also determine the global structure of the inner and outer debris disks in the [8, 600] au range, consistent with the updated orbital solution.

Unified Astronomy Thesaurus concepts: Exoplanet dynamics (490); Exoplanet systems (484); Exoplanet detection methods (489)

1. Introduction

Several approaches are being used to detect extrasolar planets. Indirect methods, such as radial velocity (Mayor & Queloz 1995), transits (Henry et al. 2000), timing (Wolszczan & Frail 1992), and classic astrometry (Muterspaugh et al. 2010), rely on studying the radiation of the central star, while the planets themselves are not observed. The imaging technique detects the planets directly, given their own infrared (IR) radiation. This method, limited by the contrast, stability, and resolution of the images, is sensitive for massive and young planets in wide orbits. Therefore, even for the nearby star HR 8799, located ∼40 pc from the Sun (Gaia Collaboration et al. 2018), it is only possible to detect the planets with long periods of 10^2–10^3 yr, as discovered by Marois et al. (2008, 2010). This makes the orbit determination a very difficult task. The measured astrometric positions of the planets relative to the star are typically uncertain to a few 0″001 (mas), but this is still not sufficient to uniquely constrain the orbits. Qualitatively different architectures are consistent with the present observations (e.g., Wertz et al. 2017). Astrometric (purely geometric) orbital models are strongly unstable (e.g., Konopacky et al. 2016; Wang et al. 2018); however, there are also reported dynamically tuned configurations which, though hardly chaotic in the Lyapunov exponent sense, can survive for hundreds of Myr (Götberg et al. 2016), comparable with the age of HR 8799 of ≃30–60 Myr (Marois et al. 2010; Wilner et al. 2018).

On the other hand, a resonant or near-resonant system resulting from the convergent migration was shown to explain the observations as well (Goździewski & Migaszewski 2014, 2018, hereafter GM14 and GM18, respectively). We justified a rigorously stable 8:4:2:1 mean-motion resonance (MMR) as the most likely architecture on dynamical grounds, consistent with the recent studies in Konopacky et al. (2016) and Wang et al. (2018). They independently found, by imposing Markov Chain Monte

Carlo (MCMC) dynamical priors, that coplanar orbits near the 8:4:2:1 MMR result in orders of magnitude more stable orbits than any other scenario and provide adequate fits to the measurements. In the present work, we extend the MMR hypothesis by linking the putative resonance chain with the planetary *N*-body periodic solutions (Hadjidemetriou 1976; Hadjidemetriou & Michalodimitrakis 1981; see also citations therein). In the later paper, they computed families of periodic orbits (POs) for the four-body planetary system and applied the results to the Galilean moons of Jupiter. This follows de Sitter's mathematical theory of the Laplace resonance in a Newtonian framework. De Sitter found a family of stable POs as the Poincaré orbits of the second kind (Broer & Hanßmann 2016). These authors also proposed that librations (quasiperiodic solutions) near these POs may provide a realistic explanation of the observations. We apply a similar reasoning to the HR 8799 system.

Because the 8:4:2:1 MMR chain in the HR 8799 system generalizes the Laplace resonance (Papaloizou 2015), there is a fairly obvious link of this prior resonant model found in GM14 and GM18, with a PO interpreted as the MMR center. Here, similar to Hadjidemetriou & Michalodimitrakis (1981), we consider a planetary system as a PO when the osculating orbital elements of the orbits are periodic in time with regard to a nonuniformly rotating reference frame tied to the osculating apsidal line of a selected planet. The present study is inspired by our finding that the 8:4:2:1 MMR configurations fitting the observations of HR 8799 are in fact very close to an exact PO of the five-body system.

Periodic configurations are known to result from smooth convergent migration in systems of two or more planets (e.g., Beaugé et al. 2006; Migaszewski 2015). In our numerical simulations of convergent migration (see GM14 and GM18), three- and four-planet MMR chains of the Laplace resonance appear naturally, in wide ranges of the migration timescales and planet masses. The migration quickly drives planets to long-term stable systems, typically in a few Myr timescale. This

indicates that the 8:4:2:1 MMR capture may be an efficient process, weakly dependent on physical conditions in the protoplanetary disk. Simultaneously, stable systems are confined to tiny, isolated islands in the orbital parameter space, as narrow as $\simeq 0.5$ au in semimajor axes and $\simeq 0.05$ in eccentricity (GM14 and GM18), and that reflects the deterministic character of the migration. Also, the increased eccentricities of the innermost planets observed in the best-fitting, stable solutions and our simulations are consistent with an early evolutionary period of convergent inward migration of all four planets, trapping them pairwise in 2:1 MMRs and pumping the orbital eccentricities while in resonance lock (Yu & Tremaine 2001; Wang et al. 2018).

Our new method improving the migration-constrained optimization (MCOA) in GM14 and GM18 relies on two attributes of periodic configurations. When modeling the data with a stable PO, the long-term dynamical stability is guaranteed per se. Also, similar to MCOA, instead of exploring large, n-dimensional parameter space, where the number of free parameters $n = 23$ for a coplanar system of four planets, including their masses and the parallax, we may limit the optimization to a p-dimensional manifold embedded in this space; here, as explained below, $p = 11$, or, if the masses and parallax are fixed (given a priori), $n = 18$ versus $p = 6$. Therefore, the MMR (periodic) constraint makes it possible to substantially reduce the number of free parameters characterizing the orbital configuration and avoid degeneracy caused by a small ratio of the data points to the degrees of freedom.

But the advantage of the PO-constrained method over the standard orbital fitting does not lie only in the reduction of the parameter space. In modeling a generic planetary configuration, the orbital elements, as well as the planetary masses, must all be free parameters, independent of one another. Therefore, the masses cannot be determined from the astrometric observations, unless they sufficiently map the orbits or are sufficiently precise to make it possible to detect mutual gravitational perturbations. In turn, the orbital elements of a periodic (exactly resonant) solution strongly depend on the planet masses and total angular momentum of the system, assuming that the linear scale of the system and the central star's mass are given (Hadjidemetriou 1976; Hadjidemetriou & Michalodimitrakis 1981). Therefore, these critical parameters may be derived with relatively short orbital arcs and independently of the planets' cooling theory. As we also show below, because the POs impose tight timing on the orbital evolution, it is already possible to indirectly measure the system parallax. The planet masses and parallax determined from the relative astrometry that are self-consistent with the astrophysically fixed stellar mass establish a test bed and benchmark for our hypothesis.

We describe the results of the PO model of the HR 8799 system in Section 2, the global structure of debris disks in Section 3, and the main conclusions in Section 4. The details and supplementary material are given in Appendices A–C.

2. Fitting the Exact Laplace Resonance

In order to test the PO hypothesis, we used the earliest Hubble Space Telescope (HST) observations in Lafrenière et al. (2009) and Soummer et al. (2011); the homogeneous, uniformly reduced data in Konopacky et al. (2016); the most recent refined Gemini Planet Imager (GPI) observations in De Rosa et al. (2020); and the most accurate detection of

HR 8799e in GRAVITY Collaboration et al. (2019) with the GRAVITY instrument. This primary set does not contain all observations available in the literature, and we limited the data in order to reduce possible observational biases due to different instruments and pipelines but extend the observational window as much as possible. This approach follows our earlier work GM18 and also Wang et al. (2018). The data set $\mathcal{D}$ consists of $N_{\rm obs} = 65$ astrometric planet positions (R.A.$_i \equiv \alpha_i$, decl.$_i \equiv \delta_i$, $i = 1, \ldots, N_{\rm obs}$) relative to the star with a mean uncertainty $\simeq 8$ mas. However, there is a particular datum from GRAVITY with (α, δ) errors as small as 0.07 and 0.2 mas, respectively. This precision detection with the optical interferometry seems to be critical for constraining the best-fitting solutions. As the epoch t_0 of the osculating initial condition, we chose the date of the first HST observation, $t_0 = 1998.829$, in Lafrenière et al. (2009) and Soummer et al. (2011). We also tested the PO model against all $N_{\rm obs} = 127$ measurements available in the literature, as listed in Wertz et al. (2017), and updated with newer or rereduced Keck, GPI, and GRAVITY points (Appendix A.2). In both cases, the fitting results and conclusions closely overlap.

Fitting a PO to the astrometric data is similar to our approach in GM14 and GM18, in which a migration-constrained coplanar solution is appropriately transformed to be consistent with the observations. Here the optimization process is essentially deterministic (fully reproducible), better constrained, regarding the masses and parallax as free parameters of the dynamical model, and CPU-efficient; computations may be performed on a single workstation. Instead of simulating the migration, for given masses $m_{\rm e}$, $m_{\rm d}$, $m_{\rm c}$, $m_{\rm b}$, and C, or, equivalently, the period ratio $\kappa = P_{\rm d}/P_{\rm e}$ of the inner pair of planets, we find a strictly periodic, coplanar resonant solution (see Appendix A for details) but with some arbitrary relative phases of the planets. Then, using the N-body dynamics scale invariance, the inferred "raw" semimajor axes are linearly rescaled with the factor ρ, the orbital plane rotated to the sky plane by three Euler angles (I, Ω, $\omega_{\rm rot}$), and the planets propagated along the PO with the N-body integrator to epoch $t_{\rm phase}$ equivalent to the first observation epoch t_0. For the given observation epochs t_i, $i = 1, \ldots, N_{\rm obs}$, the Cartesian coordinates of the planets are rescaled by the parallax Π in order to obtain the angular positions (α_i, δ_i). Then the ephemeris may be compared with the observations. To quantify that, we construct the merit function, e.g., the common χ^2 or other goodness-of-fit measure, such as the maximum-likelihood function $\mathcal{L}$ or the Bayesian posterior $\mathcal{P}$. In the most general settings, the merit function depends on 11 free parameters, $\boldsymbol{x} \equiv (m_{\rm e}, m_{\rm d}, m_{\rm c}, m_{\rm b}, \kappa, \rho, I, \Omega, \omega, t_{\rm phase}, \Pi)$, i.e., masses of the planets, period ratio of the two inner planets, linear scale factor, Euler angles, epoch, and parallax. At this point, the data modeling becomes almost the standard optimization—almost, and not really trivial, since we now must seek the best-fitting $\boldsymbol{x}$ constrained to a manifold of a stable PO family, representing the particular MMR chain. One needs to find an extremum of the merit function, as well as estimate the uncertainties of the best-fitting parameters (e.g., Gregory 2010).

Details and variants of our experiments regarding optimization on the PO manifold are described in Appendix A. Here we quote the final best-fitting parameters in Table 1. The top part of this table shows the primary fit parameters $\boldsymbol{x}$, and the bottom part is for the derived, osculating astrocentric Keplerian elements at the epoch $t_0 = 1998.829$. Uncertainties

Table 1
The Best-fitting, Strictly Periodic Model of the HR 8799 Planetary System

Parameter/Planet	HR 8799e	HR 8799d	HR 8799c	HR 8799b
Planet mass, $m\,(m_{\rm Jup})$	7.4 ± 0.6	9.1 ± 0.2	7.8 ± 0.5	5.7 ± 0.4
	7.34688506	8.97059370	7.78986828	5.85290522
Longitude of ascending node, Ω (deg)		61.85 ± 0.45		
		62.02658660		
Inclination, I (deg)		26.4 ± 0.3		
		26.55235715		
Parallax, Π (mas)		24.3 ± 0.1		
		24.36337601		
Period ratio, P_d/P_e		1.985 ± 0.002		
		1.983096		
Scale factor, ρ		1.054 ± 0.002		
		1.05177401		
Relative phase, $t_{\rm phase}$ (yr)		331.42 ± 0.13		
		331.39813970		
Rotation angle, $\omega_{\rm rot}$ (deg)		157 ± 1		
		156.38496284		
Semimajor axis, a (au)	16.25 ± 0.04	26.67 ± 0.08	41.39 ± 0.11	71.6 ± 0.2
	16.21068245	26.59727940	41.27484337	71.42244964
Eccentricity, e	0.1445 ± 0.0013	0.1134 ± 0.0011	0.0519 ± 0.0022	0.016 ± 0.001
	0.14421803	0.11377309	0.05273512	0.01587597
Argument of pericenter, ω (deg)	111.2 ± 0.6	29 ± 1	92.7 ± 0.7	42.0 ± 2.2
	111.05649395	28.35795849	92.75709369	41.35621703
Mean anomaly, $\mathcal{M}$ (deg)	−23.5 ± 0.7	60.8 ± 0.8	145.3 ± 0.9	−48.2 ± 2.1
	−23.88996589	60.75229572	144.93313134	−47.73005711

Note. Median values and the 1σ uncertainties resulting from the DE-MC sampling are given in the top row of each parameter, while values in the bottom row with more significant digits, in order to closely reproduce the PO solution, correspond to the best-fitting parameters in terms of the χ^2 statistics. Gaussian planet mass priors from the hot-start evolutionary models are $(5.8 \pm 0.5)\,m_{\rm Jup}$ for HR 8799b and $(7.2 \pm 0.7)\,m_{\rm Jup}$ for all other planets (Wang et al. 2018), and the parallax prior is (24.22 ± 0.09) mas (Gaia Collaboration et al. 2018). The first part of the table is for the primary fit parameters $\boldsymbol{x}$, and the last four rows are for the inferred osculating, astrocentric Keplerian elements at the epoch of $t_0 = 1998.829$, the first measurement in Lafrenière et al. (2009) and Soummer et al. (2011). The mass of the parent star $(1.52 \pm 0.15)M_\odot$ (Konopacky et al. 2016) is fixed at its nominal value in order to avoid the mass–orbital scale correlation. For the model with $p \equiv \dim \boldsymbol{x} = 11$ free parameters, $\chi^2 = 142.93$ and rms $\simeq 6.7$ mas.

are estimated with the help of the differential evolution Markov chain (DE-MC) method (Ter Braak 2006). The astrometric data together with the best-fitting model are illustrated in Figure 1. The left panel shows the (R.A., decl.) diagram with a close-up of the GRAVITY datum (GRAVITY Collaboration et al. 2019). In this zoom, 200 randomly chosen synthetic orbits are shown with gray curves, while black points denote the positions of the synthetic solutions in the epoch of the observation. Gray oval contours mark 1σ, 2σ, and 3σ confidence intervals stemming from the DE-MC sampling. The right panel illustrates the R.A. and decl. of the model and observations as functions of the epoch. The PO described in Table 1 yields the reduced $\chi_\nu^2 \simeq 1.24$ for $p = 11$ free parameters, $N_{\rm obs} = 65$, $\nu = 119$, and the rms $\simeq 6.7$ mas compares to the mean uncertainty of the measurements $\simeq 8$ mas. It adequately explains the data in a statistic sense. In particular, the time and sky-plane synchronization of the model with the GRAVITY data (left panel in Figure 1) is apparently perfect.

The orbital evolution of this best-fitting system, integrated for 1 Gyr, is presented in Figure 2. This figure shows orbits of HR 8799e, HR 8799d, and HR 8799c in a reference frame

corotating with HR 8799b. All trajectories are closed, consistent with the periodic evolution of the system. The positions of the planets are shown only in epochs of conjunctions between HR 8799b and HR 8799c (big filled circles), as well as their oppositions (small circles). Both the conjunctions and the oppositions repeat in the same pattern. The system is then an exact 8:4:2:1 MMR chain consisting of triple two-body 2:1 MMRs of subsequent pairs of planets, with librations of the critical angle of the zeroth-order four-body MMR $\phi_{8:4:2:1} = \lambda_e - 2\lambda_d - \lambda_c + 2\lambda_b$ (where $\lambda_{b,c,d,e}$ are the mean longitudes of the planets) with a small amplitude $\simeq 4°$ (Figure A7). It is worth noting that while the mean orbital osculating period ratios are $\simeq 2.03$, $\simeq 2.08$, and $\simeq 2.17$ for the innermost to outermost pairs of planets, respectively, the canonical (proper) mean-motion frequency (Morbidelli 2002) ratios are equal to $1/2$, indicating exact two-body 2:1 MMRs. Therefore, the MMR chain is understood as the generalized Laplace resonance. In order to illustrate the long-term stability of the model, we computed dynamical maps in terms of the mean exponential growth factor of nearby orbits (MEGNO, aka $\langle Y \rangle$; Cincotta et al. 2003) for each planet. The integration interval of 10 Myr translates to $\simeq 20{,}000$ outermost orbits,
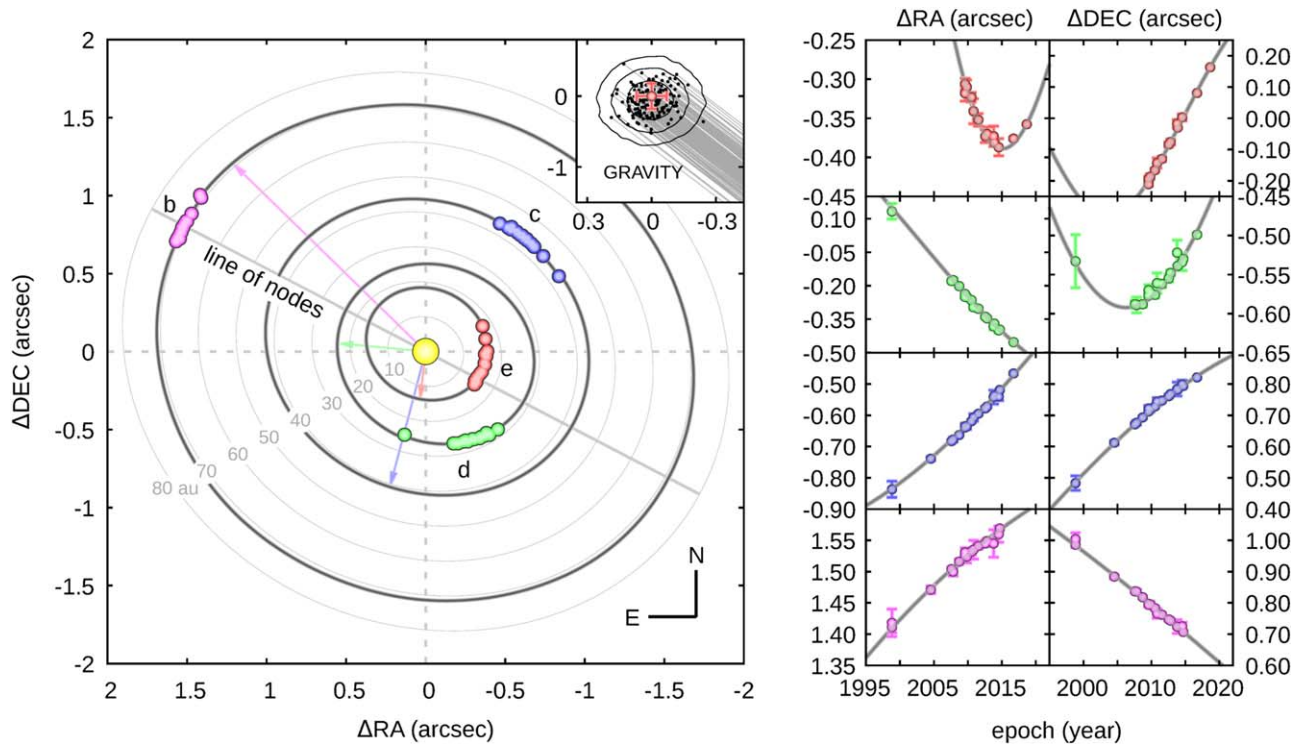
Figure 1. Astrometric observations (red, green, blue, and magenta points for planets HR 8799e, d, c, and b, respectively) in the set used for the analysis. The thick gray curves illustrate the best-fitting orbits (Table 1). The light gray curves in the left panel mark the referencing circular orbits of radii 10, 20, 30, ..., 80 au in the orbital plane of the system. The red, blue, green, and magenta arrows point to the periastron of each orbit. The close-up of the GRAVITY data is illustrated in the inset in the top right corner of the left panel. Gray curves represent 200 randomly chosen orbits from the DE-MC sampling, and black dots mark positions at the orbits in the epoch of the GRAVITY observation (2018.656). The graph is centered at the datum, and the axes are expressed in milliarcseconds. Black curves are for 1σ, 2σ, and 3σ confidence intervals for the model position at the R.A.–decl. plane at the epoch of 2018.656, derived from the DE-MC sampling. The right panel illustrates the observations and model orbits as the time functions of R.A. and decl.
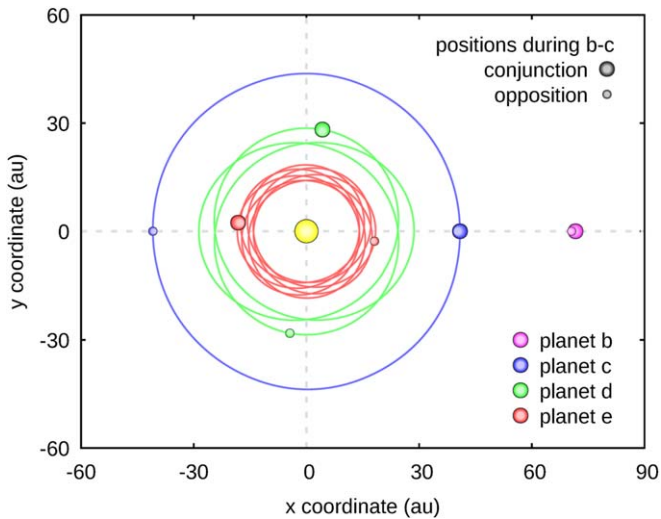

Figure 2. Astrocentric positions of the HR 8799 planets over 1 Gyr N-body integration presented in the orbital plane corotating with HR 8799b. The red, green, and blue curves illustrate the orbits of HR 8799e, d, and c, respectively. Big red, green, blue, and magenta symbols mark the positions of planets e, d, c, and b during the conjunction of planets b and c, while smaller symbols denote the positions during their opposition. The yellow symbol at the origin marks the parent star.

sufficient to detect short-term, MMR-induced instability. Remarkably, the maps (Figure A8) are similar to our earlier Figure A5 in GM14, illustrating the MCOA model built upon a

much narrower data window, and still consistent with the updated periodic model of the system.

The uncertainties of the parameters are illustrated in Figure 3 (also Figures A5 and A6 in Appendix A). The top panels are for the mass–mass diagrams. Red points with shaded ellipses indicate Gaussian priors imposed on the masses consistent with the hot-start cooling theory (Wang et al. 2018), while gray filled contours denote 1σ, 2σ, and 3σ confidence intervals of the posterior probability distributions. Apart from the HR 8799d mass, the posterior closely fits with the astrophysical constraints. The bottom left panel shows the posterior distribution of the orbital inclination and the longitude of the ascending node. These parameters exhibit substantial correlations yet are much reduced thanks to the priors. The bottom right panel is for the parallax, nominally agreeing to $\simeq 0.3\%$ with the Gaia DR2 value. The Gaussian prior on the Gaia parallax (Gaia Collaboration et al. 2018; red curve) closely overlaps with the DE-MC posterior.

3. Resonant Structure of Debris Disks

The orbits of the planets likely share a common plane with the outer debris disk (Matthews et al. 2014; Booth et al. 2016; Read et al. 2018; Wilner et al. 2018). Determination of the debris disk structure with the IR and millimeter observations is still not fully conclusive in terms of both the orientation and the inner edge r_{inner} of the disk (Booth et al. 2016). They argued that the structure of the disk might be a footprint of a fifth, as yet unseen planet beyond HR 8799b. Read et al. (2018)
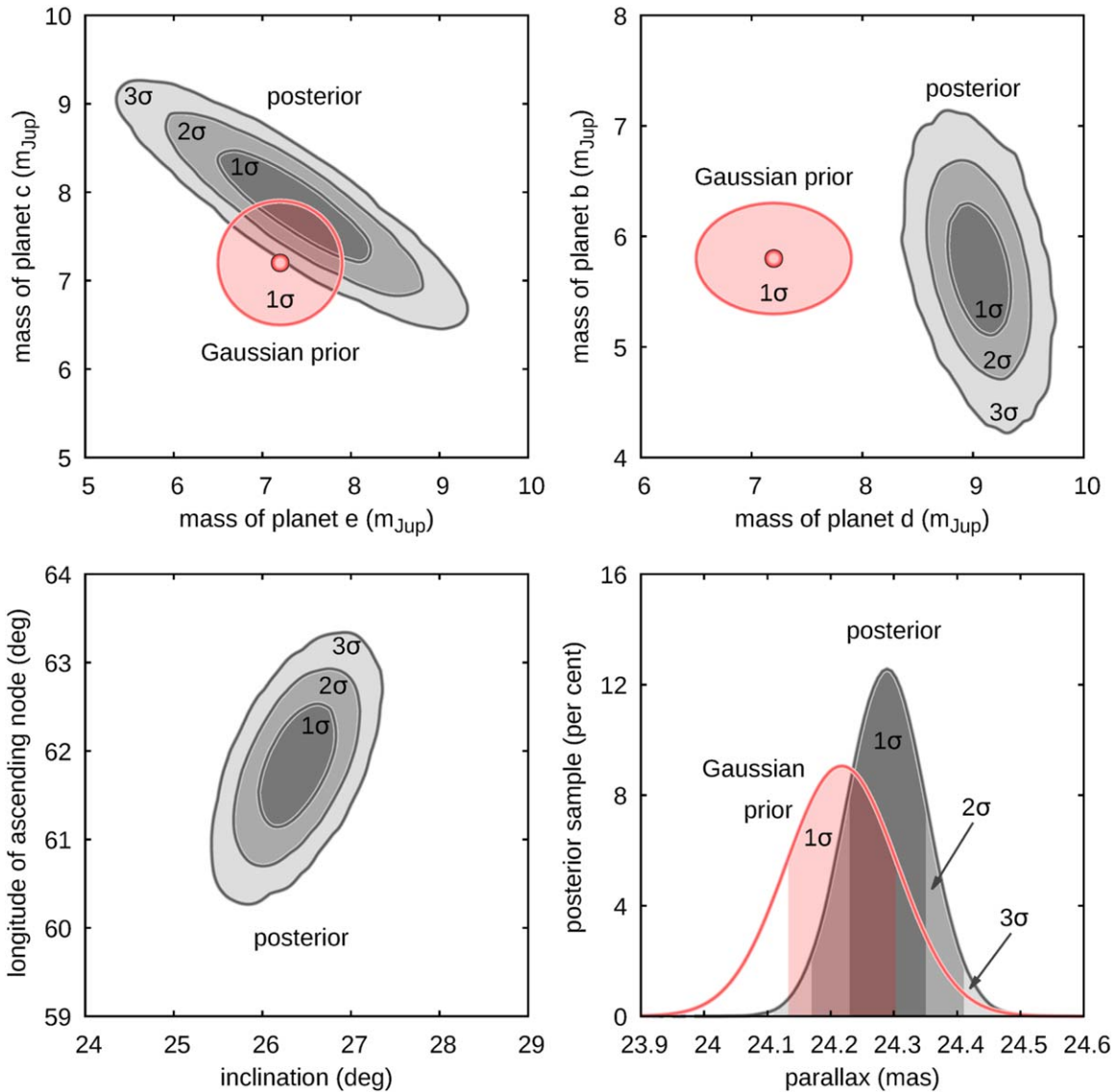
Figure 3. Posterior probability distributions of the planets' masses, inclination, longitude of the ascending node, and parallax. The shades of gray indicate the 1σ, 2σ, and 3σ confidence ranges of the parameters. Red symbols with circle/ellipse contours in the top panels show the astrophysical mass constraints (Wang et al. 2018), which are the priors in the DE-MC sampling. The red curve in the bottom right panel is the prior put on the parallax according to the Gaia DR2 catalog (Gaia Collaboration et al. 2018). See also Table 1 and its notes.

proposed such an additional planet, HR 8799f, with a mass and semimajor axis of 0.1 m_{Jup} and 138 au that could predict the outer belt's edge and explain the Atacama Large Millimeter/submillimeter Array (ALMA) observations. Later, Wilner et al. (2018), with observations at the Submillimeter Array at 1340 μm, detected the inner edge of the debris disk at 104 ($+8$, -12) au and the disk extending to $\simeq$500 au. They also constrained the mass of outer planet HR 8799b to $\simeq$6 m_{Jup}. Remarkably, it is close to our best-fitting value. Furthermore, Geiler et al. (2019) found that a single, wide planetesimal disk does not reproduce the observed emissions and proposed a two-population model, comprising a Kuiper Belt–like structure of low-eccentricity planetesimals and a scattered disk composed of a high-eccentricity population of comets.

With the new, strictly resonant configuration of the four planets, including their updated masses and the parallax, we conducted preliminary N-body simulations resulting in 3.3×10^6 small-mass asteroids that reveal the global dynamical structure of the debris disks (see Appendix C for details).

The inner border of the outer disk (Figures 4 and C2) is significantly nonsymmetric, with a nonuniform density of asteroids, which may bias the disk orientation angles derived from simple models assuming the axial symmetry. The inner edge from our simulations agrees with the observational model of Wilner et al. (2018). Moreover, we found a ring of high-eccentricity asteroids at $\simeq$140–160 au (Figure C2), close to the inner edge reported in Booth et al. (2016) and Read et al. (2018), which results in locally increased velocity dispersion. The velocity dispersion could impose a higher dust production rate and stronger emission, making the disk radial intensity profile no longer consistent with a simple power law.

4. Discussion and Future Research

Under the PO hypothesis, which is justified on dynamical and system formation grounds, the present astrometric data of the HR 8799 planets make it possible to determine not only the parallax but also the masses, independently of the cooling
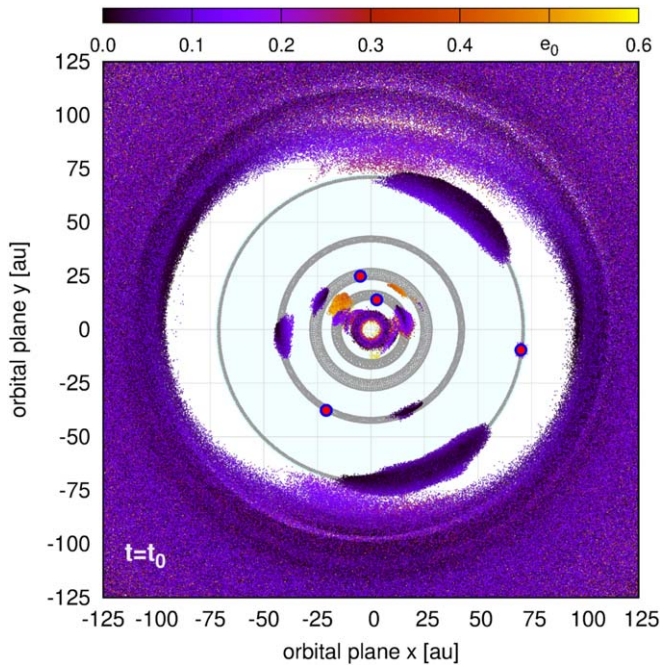
Figure 4. Inner part of the outer debris disk revealed by $\simeq 3.3 \times 10^6 \langle Y \rangle$ stable orbits found in the whole debris disk simulation, illustrated as a snapshot of astrocentric coordinates (x, y) and osculating orbital eccentricities e_0 of these orbits at the initial epoch, color-coded and labeled in the top bar. The initial positions of planets are marked with filled circles. Gray rings illustrate their orbits integrated in a separate run for 10 Myr.

Figure 5. Best-fitting value of the innermost planet with 1σ uncertainty for the data set with additional synthetic measurements given in subsequent epochs up to 2030. See the main text (Section 4) for details.

theory. In order to illustrate this prediction, we simulated new synthetic observations around the best-fitting model in Table 1 with fixed $m_e = 7\,m_{\rm Jup}$ and Gaussian noise equal to the GRAVITY data uncertainty. We performed the χ^2 minimization without the planets' mass priors, adding new synthetic measurements after the last epoch of each planet. The resulting time series of the best-fitting m_e and its 1σ range indicate (Figure 5) that with merely one more epoch, $\simeq 2020.5$, all masses become meaningfully constrained without prior information. If the HR 8799 system is indeed represented by a PO or a nearby stable resonant configuration, then it may be possible to determine the planets' masses based solely on the relative astrometry. This could be a test bed for the cooling theory of HR 8799 system–like massive planets, and (possibly) such planets in other multiple systems discovered via direct imaging. The deterministic PO model may serve as a reference configuration useful for the astrometric and physical characterization of such resonant or close-to-resonant systems.

The PO hypothesis may be naturally confronted with compact multiple Kepler and super-Earth systems that are predominately close to but not actually inside of MMRs (e.g., Fabrycky et al. 2014). The planetary migration might easily generate resonant states but does not preferentially retain small planets in such states. From this perspective, the PO of HR 8799 might not be necessarily preferred over near-MMR (possibly weakly chaotic) configuration, with the Lagrangian (geometric) stability timescale exceeding the age of the system. But the tight observational constraints invoked here seem to contradict that. Moreover, Ramos et al. (2017) argued that 2:1 MMR systems relatively distant from the star, such as HD 82943 and HR 8799, are characterized by very small resonant offsets, while higher offsets are typical of short-period Kepler systems. Achieving an exact MMR versus near-MMR state
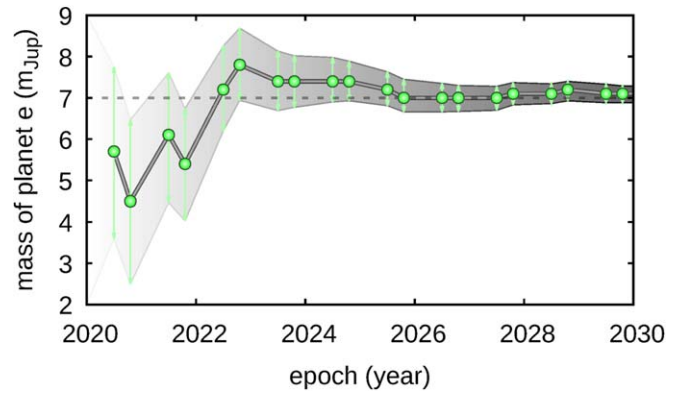
likely depends on the differing efficacy of resonant retention of four enormous giant planets versus much smaller Kepler planets and different formation of such systems. Wide-orbit systems require long formation timescales that are furthermore inconsistent with type II migration characteristic of massive planets. Alternatively, pebble accretion initially accompanying type I migration (Johansen & Lambrechts 2017) or new paradigms of type II migration (Ida et al. 2018) may explain the putative MMR chain. Therefore, the confirmed PO of the HR 8799 planets could be the border condition and a footprint of the system migration, shedding more light on its uncertain origin.

As the bottom line, we note that the self-consistent model of the HR 8799 system and our predictions may be verified shortly, during the next few years.

Appendix A
Numerical Setup and Algorithms

A.1. Searching for Periodic Configurations

A coplanar orbital configuration of a planetary system is determined by a vector containing the positions and velocities of the planets $\{x_i, y_i, u_i, v_i\}$ or, equivalently, consisting of astrocentric Keplerian elements of the orbits $\{a_i, e_i, \varpi_i, \mathcal{M}_i\}$, i.e., the semimajor axis, eccentricity, pericenter longitude, and mean anomaly, respectively, where $i = $ e, d, c, b or, equivalently, 1, 2, 3, and 4. Both state vectors are given at a particular epoch, and the state of the system at another epoch may be obtained through propagating the initial condition with the numerical integration of the N-body equations of motion. A configuration of the planetary N-body problem is called periodic if, after time interval T (called the period of PO), it returns to its initial state in the reference frame rotating nonuniformly with the temporal (osculating) pericenter of a selected planet (Hadjidemetriou 1976). For the Keplerian representation of orbits, we have the boundary conditions: $a_i(T) = a_i(0)$, $e_i(T) = e_i(0)$, and $\mathcal{M}_i(T) = \mathcal{M}_i(0)$ for all orbits. Since the angular momentum C of the system must be conserved, the pericenter longitudes $\varpi_i(T) \neq \varpi_i(0)$. However,

$\Delta\varpi_{i,j} \equiv \varpi_i - \varpi_j (i \neq j)$ must be the same after T, $\Delta\varpi_{i,j}(T) = \Delta\varpi_{i,j}(0)$. This means that the relative configuration of the planets remains fixed after the period, while the whole system rotates by a certain angle around its angular momentum vector aligned with the z-axis (e.g., Lithwick et al. 2012).

Here we consider the evolution of the Keplerian elements to be periodic in a reference frame corotating with the apsidal line of the innermost orbit; the reference orbit can be chosen freely. Equivalently, when considering the Cartesian coordinates, one needs to search for configurations whose positions and velocities expressed in a reference frame corotating with one of the planets $(\bar{x}, \bar{y}, \bar{u}, \bar{v})$ fulfill the periodicity conditions $\bar{x}_i(T) = \bar{x}_i(0)$, $\bar{y}_i(T) = \bar{v}_{x,i}(0)$, and $\bar{v}_{y,i}(T) = \bar{v}_{y,i}(0)$ (Hadjidemetriou 1976). We used this Cartesian representation, common in the literature, only for an illustration (see Figure 2); note that in this case, we chose the outermost planet as the reference one.

For the given planet masses, there exist families of periodic configurations parameterized by total angular momentum or a value of the osculating period ratios of one of the planet pairs in a chosen phase of the evolution (Hadjidemetriou 1976; Hadjidemetriou & Michalodimitrakis 1981). To select a particular family, we fix the period ratio of the innermost pair at the epoch in which the innermost planet resides in its pericenter. We denote this period ratio as parameter $\kappa = (P_d/P_e)|_{\mathcal{M}_e=0}$. Formally, for a chain of the 8:4:2:1 MMR, there are eight different epochs in which the innermost planet is in the pericenter. We select one of them and keep this choice when continuing a given family with regard to other parameters of the solution, denoted as a generic parameter vector $\boldsymbol{x}$.

After testing various parameterizations of the PO in terms of numerical efficiency and reliability, we decided to use the following set of components of the state vector $\boldsymbol{X}$, each of which is a function of the astrocentric, osculating Keplerian elements: $X_1 = \log_{10} e_e$, $X_2 = \log_{10} e_d$, $X_3 = \log_{10} e_c$, $X_4 = \log_{10} e_b$, $X_5 = P_c/P_d - (P_c/P_d)_{\text{nom}}$, $X_6 = P_b/P_c - (P_b/P_c)_{\text{nom}}$, $X_7 = \varpi_e - \varpi_d$, $X_8 = \varpi_d - \varpi_c$, $X_9 = \varpi_c - \varpi_b$, $X_{10} = \mathcal{M}_d$, $X_{11} = \mathcal{M}_c$, $X_{12} = \mathcal{M}_b$, where

$$(P_c/P_d)_{\text{nom}} = [1 + C_0\{1 - (P_d/P_e)\}]^{-1},$$
$$(P_b/P_c)_{\text{nom}} = [1 + C_1\{1 - (P_c/P_d)_{\text{nom}}\}]^{-1},$$
$$C_0 = \frac{j\,q}{i(p+j)},$$
$$C_1 = \frac{k\,p}{j(r+k)}. \qquad (A1)$$

The nominal values of the period ratios $(P_c/P_d)_{\text{nom}}$ and $(P_b/P_c)_{\text{nom}}$ correspond to a chain of exact MMRs (Delisle 2017), $P_d/P_e \approx (q+i)/q$, $P_c/P_d \approx (p+j)/p$, $P_b/P_c \approx (r+k)/r$. Therefore, for the case of the 2:1, 2:1, and 2:1 MMR chain, both the factors $C_0 = C_1 = 1/2$. Although the relations given above were designed for weakly interacting systems whose evolution is well described with the averaging approach (Delisle 2017), we found that such a representation enables appropriately controlling the period ratios.

For a fixed period ratio κ and masses m_e, m_d, m_c, and m_b parameterizing a given family of POs, a member of the PO family is being searched for with the Newton method for nonlinear equations (Press et al. 2002) in 12-dimensional $\boldsymbol{X}$ space. Since $\Delta X_i \equiv X_i(T) - X_i(0)$, where T is fixed so the innermost planet completes exactly eight full revolutions

(counted from its pericenter to pericenter), the set of nonlinear equations to be solved reads as $\Delta X_i(X_1, X_2, ..., X_{12}) = 0$, where $i = 1, ..., 12$. At first, the starting point is drawn randomly, yet around X_5, $X_6 \simeq 0$ (or close to an approximate solution, which we already know, such as the 8:4:2:1 MMR fits found in GM14 and GM18) until the algorithm finds a solution with $\Delta X_i \approx 0$. Next, this solution can be continued for changed κ and the planet masses. In general settings, the continuation of the PO is a complex problem, since many stable and unstable families may exist in different parameter ranges (Hadjidemetriou & Michalodimitrakis 1981, and references therein).

A.2. Data Fitting on the Parametric Grid of the PO

At the first attempt, we performed the optimization similarly to the MCOA variant in GM18. Here, instead of CPU-demanding migration simulations, which result in resonant but not necessarily periodic systems, we continued POs in a five-dimensional $\boldsymbol{Z}$ grid ($Z_1 = m_e$, $Z_2 = m_d$, $Z_3 = m_c$, $Z_4 = m_b$, $Z_5 = \kappa$), and we found $\sim 10^7$ configurations covering the interesting region of the 8:4:2:1 MMR chain. In this sense, we obtained the exactly resonant (periodic) configurations that might fit the observations as well, each being the 8:4:2:1 MMR center for different masses and the inner orbit period ratio. From this point, the analysis is essentially similar to GM18. In order to fit a given PO to the measurements, one needs to find a minimum of χ^2 in a few-dimensional space of model parameters. We performed the optimization experiments using the same parameters as in GM18: the scale parameter ρ, the phase of a periodic configuration corresponding to the reference epoch t_{phase}, and the 3-1-3 Euler angles (I, Ω, ω_{rot}), fixing the orientation of the orbital plane with regard to the sky (observer) frame. In such settings, χ^2 (equivalently, the maximum likelihood $\mathcal{L}$) depends on $\boldsymbol{Y}$, whose components are $Y_1 = \rho$, $Y_2 = t_{\text{phase}}$, $Y_3 = \Pi$, $Y_4 = I$, $Y_5 = \Omega$, and $Y_6 = \omega_{\text{rot}}$. We also updated the parameter vector $\boldsymbol{Y}$ by the system parallax Π and the so-called "error floor" $\sigma_{\alpha,\delta}$, rescaling the nominal uncertainties, in order to account for possibly underestimated errors and biases of the observations.

The merit function $\mathcal{L}(\boldsymbol{Y})$ is defined for this variant of parameterization as follows:

$$\ln \mathcal{L}(\boldsymbol{Y}) = -\frac{1}{2}\chi^2(\boldsymbol{Y}) - \sum_{i=1}^{N_{\text{obs}}}[\ln\theta_{i,\alpha} + \ln\theta_{i,\delta}] \qquad (A2)$$
$$- N_{\text{obs}}\ln(2\pi),$$

$$\chi^2(\boldsymbol{Y}) = \sum_{i=1}^{N_{\text{obs}}}\left[\frac{[\alpha_i - \alpha(t_i, \boldsymbol{Y})]^2}{\theta_{i,\alpha}^2} + \frac{[\delta_i - \delta(t_i, \boldsymbol{Y})]^2}{\theta_{i,\delta}^2}\right], \qquad (A3)$$

where (α_i, δ_i) are the measurements at time t_i; $\alpha(t_i, \boldsymbol{Y})$, $\delta(t_i, \boldsymbol{Y})$ are the ephemeris values; $\sigma_{i,\alpha}^2$ and $\sigma_{i,\delta}^2$ are the nominal measurement uncertainties in R.A. and decl. scaled in quadrature with the error floor, $\theta_{i,\alpha}^2 = (\sigma_{i,\alpha}^2 + \sigma_{\alpha,\delta}^2)$ or $\theta_{i,\delta}^2 = (\sigma_{i,\delta}^2 + \sigma_{\alpha,\delta}^2)$, for each datum, respectively; and N_{obs} is the number of observations. Also, $N = 2N_{\text{obs}}$, since R.A. and decl. are measured in a single detection. The $\ln\mathcal{L}$ function in Equation (A2) is defined in such a way that assuming the uncertainties are Gaussian and uncorrelated, the resulting best-fitting models should yield the reduced $\chi^2_\nu \simeq 1$. The merit function was optimized with the help of genetic and evolutionary algorithms (Izzo et al. 2012).

In order to illustrate the results of the PO-grid approach, we invoke a particular experiment in which we fitted the $\ln\mathcal{L}$
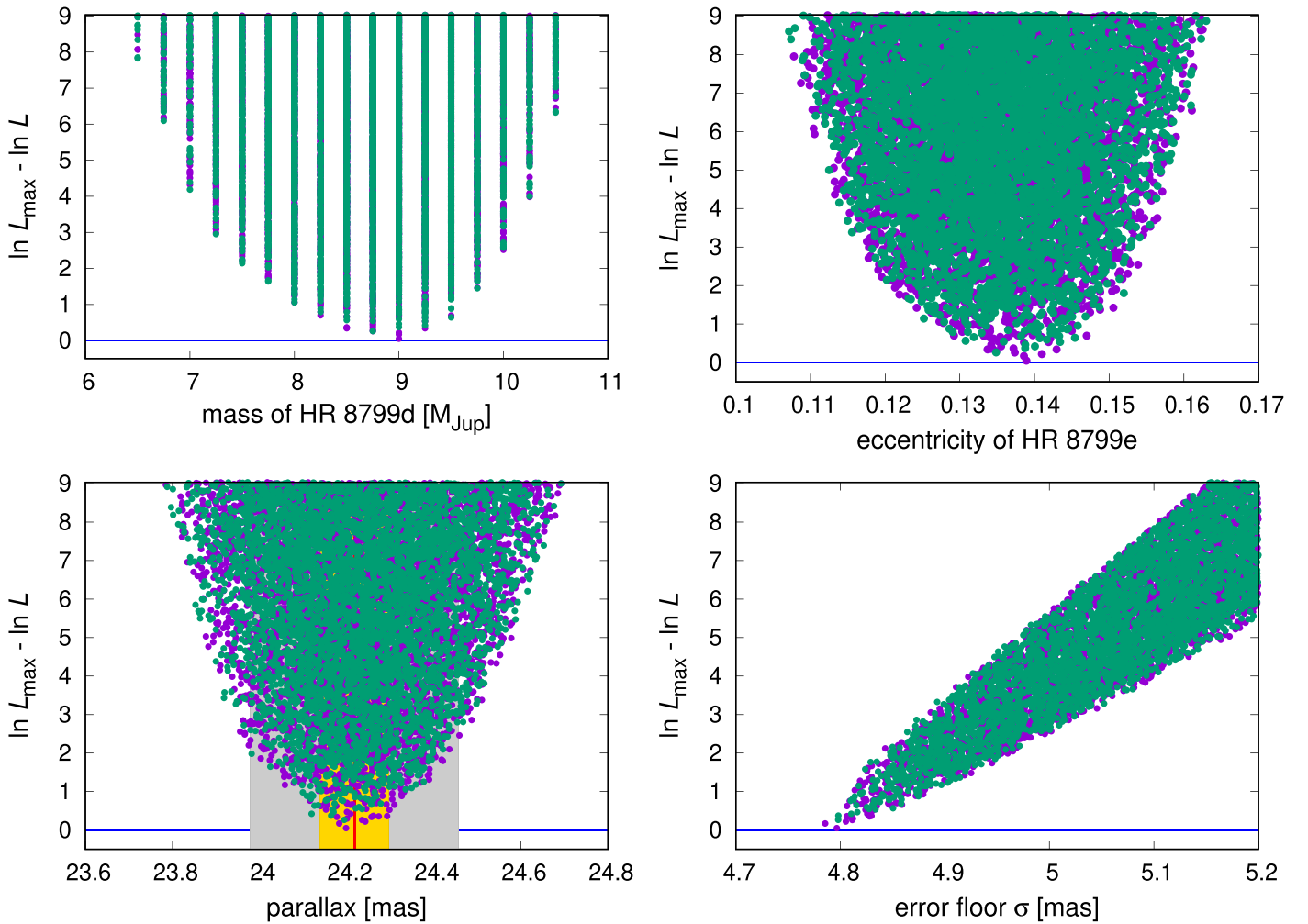
Figure A1. Plots illustrating the PO-grid search for the best-fitting parameters to astrometric measurements of the HR 8799 system. In this experiment, we fitted seven free parameters, including the orbit scale ρ, three Euler angles, the initial epoch, the system parallax Π, and the error floor σ_α, β, to all measurements gathered in the literature, $N_{obs} = 127$ data points. We optimized the likelihood function $\ln \mathcal{L}$ with the error floor term and without any priors. The extremum of $\ln \mathcal{L} \simeq -834.4$, and the error floor $\simeq 4.8$ mas. Fitted systems in two Monte Carlo sampling runs on the PO grid are marked with filled circles and different colors. Top left panel: mass of HR 8799d with a clear extremum. Top right panel: inferred eccentricity of HR 8799e from the PO models. Bottom left panel: system parallax, with the Gaia DR2 nominal value (red line) marked with its 1σ (gold rectangle) and 3σ (gray rectangle) confidence intervals. Bottom right plot: error floor $\sigma_{\alpha,\delta}$, as the global correction factor of the measurement uncertainty, yielding the reduced $\chi^2_\nu \simeq 1$.

function in Equation (A2) to all measurements available at the moment in the literature: the early HST data in Lafrenière et al. (2009) and Soummer et al. (2011), a homogeneous data set in Konopacky et al. (2016), GPI data in Wang et al. (2018), and the GRAVITY measurement in De Rosa et al. (2020), updated with mostly VLT/SPHERE, Subaru, and LBT data collected in Wertz et al. (2017) from Metchev et al. (2009), Hinz et al. (2010), Bergfors et al. (2011), Galicher et al. (2011), Currie et al. (2011, 2012, 2014), Esposito et al. (2013), Maire et al. (2015), Pueyo et al. (2015), and Zurlo et al. (2016). This set consists of $N_{obs} = 127$ (R.A., decl.) observations, some of them clearly deviating from any astrometric model. Because preliminary PO and MCOA fits indicated the reduced $\chi^2_\nu \simeq 2.5$ for the best-fitting models, we introduced the error floor $\sigma_{\alpha,\delta}$ in order to account for possible data biases and unmodeled errors.

The results are illustrated in Figure A1, which shows selected fitted parameters that are gathered on the precomputed PO grid and plotted versus $\Delta \ln \mathcal{L} \equiv \ln \mathcal{L}_{max} - \ln \mathcal{L}$, relative to the best-fitting value $\ln \mathcal{L}_{max}$ found in the search. Most of the primary Y parameters, such as the masses of HR 8799d (top left panel) and HR 8799b (not shown), the error floor $\sigma_{\alpha,\delta}$

(bottom right panel), and the system parallax (bottom left panel) exhibit clear extrema. Also, the PO-constrained eccentricities (such as for HR 8799e; top right panel) are quasi-parabolically bounded. We found it particularly surprising that the masses of HR 8799d and HR 8799b could be potentially constrained, although the $\ln \mathcal{L}$ extremum is apparently shallow. That also regards the parallax Π, which, as the free parameter of the astrometric model, overlaps with the Gaia DR2 trigonometric parallax $\Pi \simeq (24.22 \pm 0.09)$ mas within its formal 1σ uncertainty; our best-fitting value $\Pi \simeq 24.25$ mas is accurate to the fourth significant digit ($\simeq 0.1\%$, in other fits up to $\simeq 0.3\%$). We consider this as a meaningful benchmark of the self-consistency of the astrometric model, the parallax, and the physical characteristics of the system: the derived masses of the planets and the adopted stellar mass of $1.52 M_\odot$ (Konopacky et al. 2016). We note that the stellar mass must be fixed or tightly constrained, since otherwise it would introduce a strong mass–period (linear scale) correlation through the Keplerian law (actually, the N-body dynamics scaling).
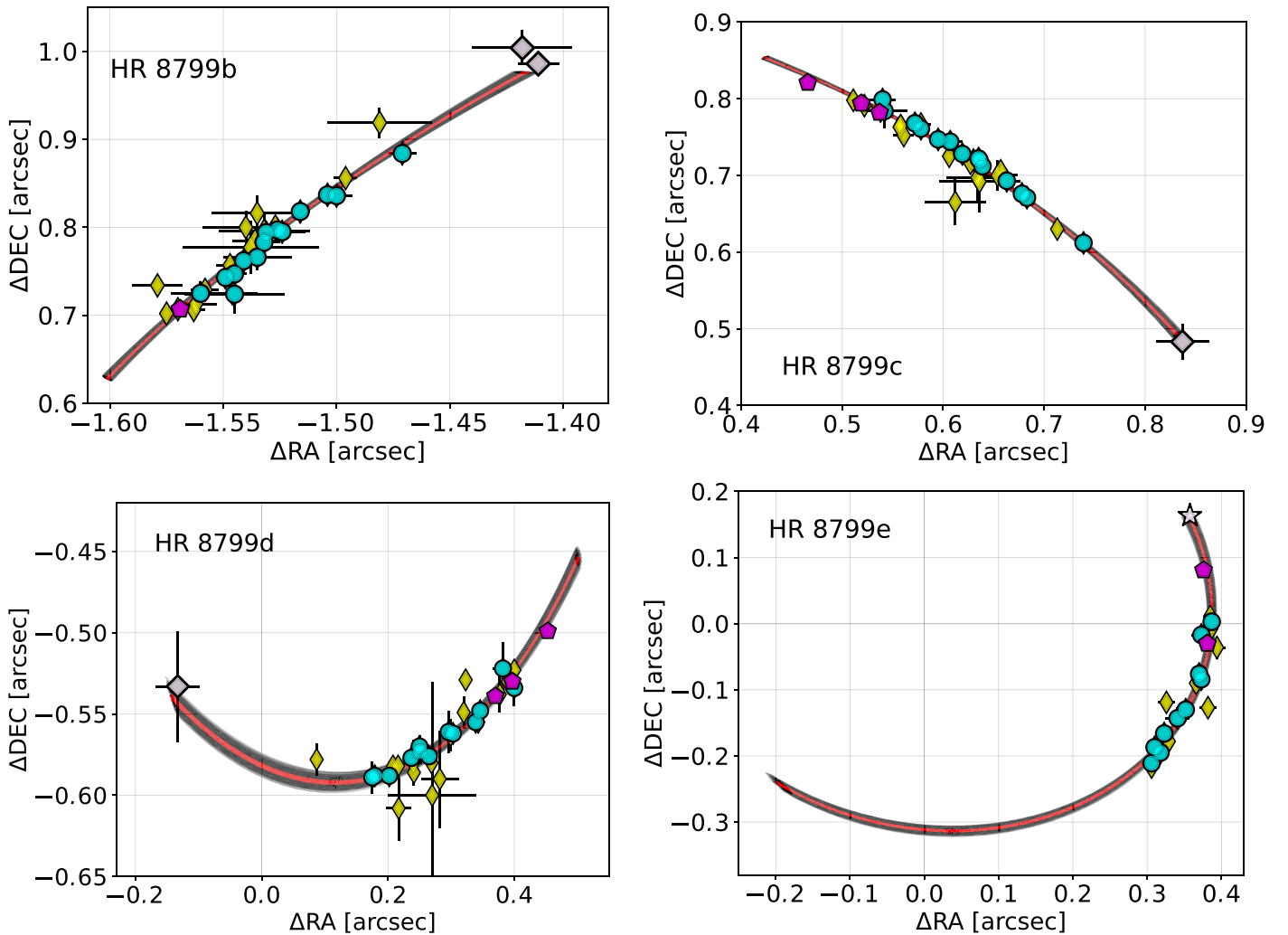
Figure A2. A PO model of all HR 8799 observations in the literature (see the text for details). Big gray diamonds are for the earliest HST data in Lafrenière et al. (2009) and Soummer et al. (2011), circles are for the uniformly reduced data set in Konopacky et al. (2016), the star symbol is for the GRAVITY measurement in De Rosa et al. (2020), pentagons are for GPI data in Wang et al. (2018), and diamonds are for the VLT/SPHERE, Subaru, and LBT data collected in Wertz et al. (2017). Black curves illustrate synthetic orbits in the sky plane, derived from the PO-grid search and plotted between epochs $t_0 = 1998.829$ and $t = 2018.654$ of the GRAVITY data for $\ln \mathcal{L} < -825.0$, and the red curves are for solutions providing $\ln \mathcal{L} < -834.0$; see Figure A1. Subsequent panels are for close-ups of the data and orbital arcs for each planet. Note that ΔR.A. is labeled negative with regard to the R.A. direction.

The orbital geometry of the best-fitting models is illustrated in Figure A2. Panels are for the close-ups of the sky plane for subsequent planets, with all data points marked with symbols for different subsets and gray curves for 250 random solutions drawn within $\simeq$1 mas range around the best-fitting models (illustrated with the red curves) and yielding $\ln \mathcal{L}$ marginally worse than the extremum value. The orbits are plotted for the time interval between $t_0 = 1998.829$ and the last GRAVITY epoch. The $\Delta \ln \mathcal{L}$ range in Figure A1 translates to a substantial spread of the models, which is most visible for HR 8799d. Although we did not compute formal confidence intervals, the spread indicates sensitivity of $\Delta \ln \mathcal{L}$ to a variation of the parameters.

The orbits plotted globally (Figure A3) for the osculating orbital period of each planet separately appear well bounded, and this is particularly apparent for the innermost, fast-moving planets. The model might predict their geometric positions close to the best-fitting PO motion for a long time, in spite of the parameter uncertainties.

The bad message received from the PO-grid fitting is a strong anticorrelation between the masses of HR 8799c and e

(m_c, m_e); moreover, the best-fitting configurations exhibit a very small innermost mass, $m_e \simeq 0.1 m_{\rm Jup}$. The grid method also depends on the resolution, which should be individually tuned for each parameter in five-dimensional space, as illustrated in the HR 8799d mass scan (top left panel in Figure A1). We found that the error floor does not help in eliminating or even reducing the mass correlation.

These preliminary PO-grid experiments provide interesting and useful hints for the final approach, described below (Appendix A.3), yet we could not consider them as fully conclusive. Unfortunately, the parametric grid approach is tedious and introduces large CPU overhead. The PO continuation and sampling must be multidimensional, and that implies not only the need for computing huge sets of solutions but also optimizing the initial conditions one by one—although we instead performed the Monte Carlo search on the grid. Determining the best-fitting model to the present observations is also difficult due to the (m_c, m_e) anticorrelation. Getting rid of that degeneracy needs additional prior information, such as the planet masses estimated on the grounds of the thermodynamical evolution and cooling tracks.
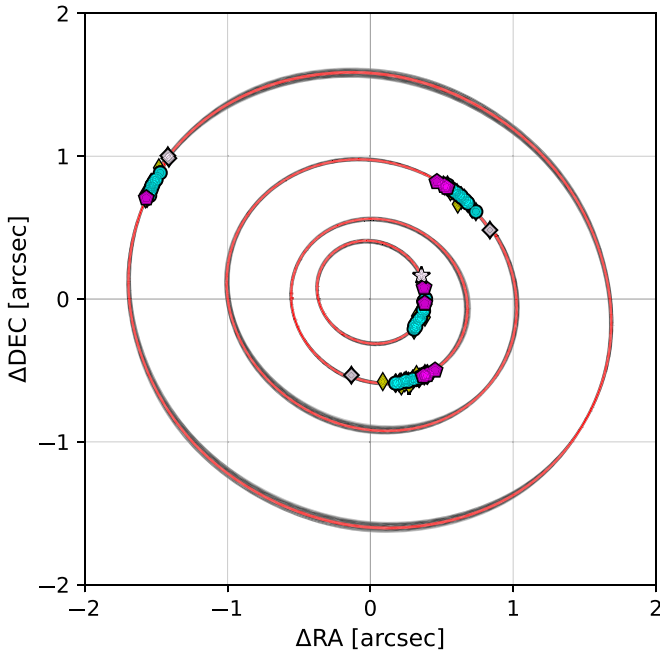
Figure A3. Global view of the HR 8799 system geometry in the plane of the sky for all data in the literature and the astrometric model derived in the PO-grid search; see caption of Figure A2.

In order to address these issues, we improved the grid MMR-constrained optimization in ways that made it CPU-efficient and independent of the grid resolution, described below. In the final experiments, we examined the reduced data set (hereafter $\mathcal{D}$) comprised of HST data in Lafrenière et al. (2009) and Soummer et al. (2011), a homogeneously reduced data set in Konopacky et al. (2016), and GPI data in Wang et al. (2018) derived with a similar instrument, as well as the GRAVITY data in De Rosa et al. (2020). We used the HST and GRAVITY data to extend the time window of the observations. For this set, we did not consider the error floor, since the PO models with the basic $p = 11$ free parameters yield $\chi_\nu^2 \simeq 1.25$ and rms $\simeq 7$ mas, consistent with the mean uncertainty of the measurements in the reduced set, $\simeq 8$ mas.

A.3. Optimization on a Manifold of Periodic Configurations

From a mathematical point of view, our goal is to find the best-fitting PO in the space of vectors $\mathbf{Z} = (m_e, m_d, m_c, m_b, \kappa)$. We note that the single κ period ratio of the innermost pair of planets is sufficient to identify the required PO, since we seek the PO in a small range around the nominal remaining period ratios, X_5 and X_6, with fixed MMR factors C_0 and C_1. As explained before, in the MCOA-like optimization, the space of vector $\mathbf{Z}$ is explored in a grid of precomputed POs. Unfortunately, even in the five-dimensional space of $\mathbf{Z}$, the number of solutions to be data-fitted becomes huge. Moreover, the mass anticorrelation with m_e tending toward very small and nonrealistic values implies a difficulty in estimating the parameter ranges of the grid, as well as its resolution. Even if we reach the neighborhood of the merit function's extremum, it is difficult to find and tune the proper grid resolution for all parameters of the model, and the five-dimensional PO grid must be updated in subsequent iterations. Still, the method is useful in investigating the parameter space in wide ranges and provides a good starting point (solutions) for a more refined and accurate method.

Clearly, a mathematically correct algorithm must explore the model parameter subspace (a manifold) fixed by the requirement of a PO. In order to implement this manifold fitting, for a given (prescribed) $\mathbf{Z}$, a coplanar PO is searched for, resulting in the Cartesian state vector $\mathbf{X}$. Next, we select the best-fitting parameters as a vector $\mathbf{Y}$ in the orbital and geometric element space. In this way, for the given $\mathbf{Z}$, the objective function, such as $\chi^2 = \chi^2(Z_1, Z_2, Z_3, Z_4, Z_5)$, is optimized under the assumptions that (i) the model orbits are periodic and (ii) the POs are optimized through the linear scaling, time-phasing, distance (parallax), and spatial orientation ($\mathbf{Y}$). We closed the whole algorithm in a single procedure, being a numerical implementation of the merit function for the optimization of $\mathbf{Z}$. Both steps that consist of continuing the PO and its final fitting to the data in the $\mathbf{Y}$ and $\mathbf{Z}$ spaces equivalent to the 11-dimensional vector of sampled parameters $\mathbf{x} = (Z_1, Z_2, Z_3, Z_4, Z_5, Y_1, Y_2, Y_3, Y_4, Y_5, Y_6)$, explicitly $\mathbf{x} = (m_e, m_d, m_c, m_b, \kappa, \rho, I, \Omega, \omega_{rot}, t_{phase}, \Pi)$, are being done with the help of the Levenberg–Marquardt (LM) algorithm (Press et al. 2002). The iterative scheme enables us to find the best-fitting PO in a small number of steps, typically a few tens of iterations.

A.4. DE-MC Sampling and Uncertainties of the Best-fitting Parameters

In order to assess realistic uncertainties and investigate possible parameter correlations, we performed the DE-MC sampling (Ter Braak 2006). Recalling some well-known elements of the Bayesian statistics and the MCMC sampling (e.g., Gregory 2010), we consider the posterior probability distribution $\mathcal{P}(\mathbf{x}|\mathcal{D}) \sim \mathcal{L}(\mathcal{D}|\mathbf{x})P(\mathbf{x})$, where $\mathcal{D}$ denotes the data set, $\mathcal{L}(\mathcal{D}|\mathbf{x})$ represents a probability that parameters $\mathbf{x}$ explain the data set $\mathcal{D}$, and $P(\mathbf{x})$ is the prior information imposed on $\mathbf{x}$. We define the $\ln \mathcal{L}$ function the same as in Equation (A2),

$$\ln \mathcal{L}(\mathcal{D}|\mathbf{x}) = -\frac{1}{2}\chi^2(\mathbf{x}) - \sum_{i=1}^{N_{obs}} [\ln \sigma_{i,\alpha} + \ln \sigma_{i,\delta}]$$
$$- N_{obs} \ln (2\pi) \equiv -\frac{1}{2}\chi^2(\mathbf{x}) + \text{const}, \quad \text{(A4)}$$

but skipping the error floor, since we performed the MCMC sampling on the reduced data set $\mathcal{D}$ described in Section 2, and for these measurements, the best-fitting models yield $\chi_\nu^2 \sim 1$—there is no need to account for the uncertainty correction.

The DE-MC sampling, which is a variant of the canonical Metropolis–Hastings algorithm, occurs according to the probability of moving from a starting point $x_1^{(i)}$ to a new point $x_2^{(i)}$ in the parameter space, $p(x_2^{(i)}|x_1^{(i)})$, which is a product of $q(x_2^{(i)}|x_1^{(i)})$ and $\alpha(x_1^{(i)}, x_2^{(i)})$, where $q(x_2^{(i)}|x_1^{(i)})$ is the probability of choosing a candidate point $x_2^{(i)}$ when starting from $x_1^{(i)}$. The superscript denotes the ith chain from a population of $n = 100$ chains that are evolved in parallel. The candidate point of the ith chain is chosen according to

$$x_2^{(i)} = x_1^{(i)} + \gamma(x_1^{(j)} - x_2^{(k)}) + \text{Uniform}(-\Delta^{(i)}, +\Delta^{(i)}), \quad \text{(A5)}$$

where the chains j and k ($j \neq k$ and $j, k \neq i$) are chosen randomly, while $\Delta^{(i)}$ is chosen individually for each parameter. In order to obtain an $\simeq 50\%$ acceptance rate, we chose $\gamma = 0.3$, and $\Delta^{(i)}$ was ($10^{-4} m_{Jup}$, $1.7 \times 10^{-4} m_{Jup}$, $1.5 \times 10^{-4} m_{Jup}$, $7 \times 10^{-4} m_{Jup}$, 5×10^{-7}, 5×10^{-5} yr, 1.2×10^{-6}, 10^{-4} mas,
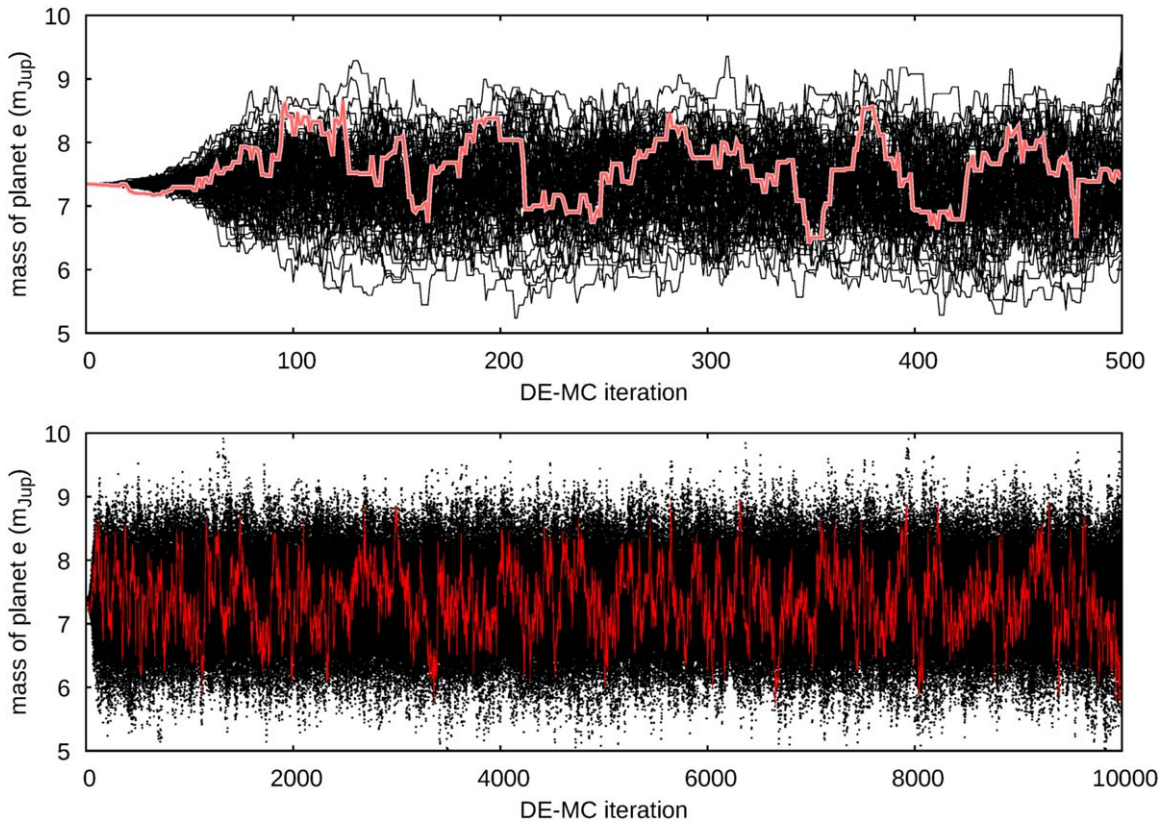
Figure A4. The DE-MC sampling for the mass of HR 8799e. Black curves indicate the evolution of all 100 individual chains, while the red curves illustrate the behavior of one chosen chain. The first 200 steps are treated as burn-in steps. The total number of iterations is 10,000; in the top panel, the first 500 steps are shown for clarity.

1.2×10^{-5} deg, 5×10^{-6} deg, 5×10^{-6} deg) for subsequent components of $\boldsymbol{x}$ (see the previous subsection). The second term in Equation (A5) is the Metropolis–Hastings ratio,

$$\alpha(x_1^{(i)}, x_2^{(i)}) = \min\left[1, \frac{\mathcal{P}(x_2^{(i)})}{\mathcal{P}(x_1^{(i)})}\right], \qquad (A6)$$

which denotes the acceptance probability of $x_2^{(i)}$ when starting from $x_1^{(i)}$. Importantly, the DE-MC algorithm propagates a number of Markov chains in parallel, starting from different initial positions in the parameters space, and introduces mixing of the solutions in the chains through the differential evolution (Price et al. 2005). That makes this algorithm both simple and computationally efficient. We also note that the DE-MC approach is crucial for our optimization problem, given the need of computationally complex PO continuation with regard to model parameters, since the PO cannot be updated sufficiently freely, as required by the Markov chain propagation.

Priors $P(\boldsymbol{x})$ for the masses were set as Gaussian with mean values and standard deviations according to Wang et al. (2018), from the hot-start evolutionary models, to $(5.8 \pm 0.5)\, m_{\rm Jup}$ for HR 8799b, and $(7.2 \pm 0.7)\, m_{\rm Jup}$ for all other planets. Similarly, the parallax Gaussian prior is $\Pi = (24.22 \pm 0.09)$ mas (Gaia Collaboration et al. 2018). For the six remaining parameters, the prior distributions were uniform in sufficiently wide ranges.

We initiated the DE-MC sampling by choosing 100 solutions from the vicinity of the best-fitting model in Table 1. The evolution of the whole population of Markov chains is illustrated in Figure A4 with black curves, while one selected example chain is depicted with red curves. At the beginning (first $\sim$100 iteration steps), all of the chains evolve close to the initial condition. Since the differences $x_1^{(j)} - x_2^{(k)}$ increase, the sampling begins to occur over a wider part of the parameter space. After $\sim$200 steps, the chain is already burned out. Those first 200 steps were not included in the final statistics of solutions obtained after 10,000 iterations. In this DE-MC experiment, we did not estimate the autocorrelation time for the Markov chains, since clearly, the relatively small number of iterations already leads to a smooth approximation of the posterior. Also, as illustrated in Figure A4, each of the chains quickly reaches the random-walk state and explores the whole parameter space. Remarkably, this behavior is much different from the MCMC sampling with the full Keplerian or even N-body models (e.g., Konopacky et al. 2016; Wertz et al. 2017; Wang et al. 2018, GM18, and references therein), which notoriously exhibit parameter correlations and long autocorrelation times $\sim 10^5$, due to multimodal posteriors and ill-constrained optimization problems implied by a small ratio of the measurements to the number of free parameters and narrow time window of the data.

According to the final results of the DE-MC sampling, as well as the scans of χ^2 function, the best-fitting configuration is meaningfully constrained with regard to all parameters. In
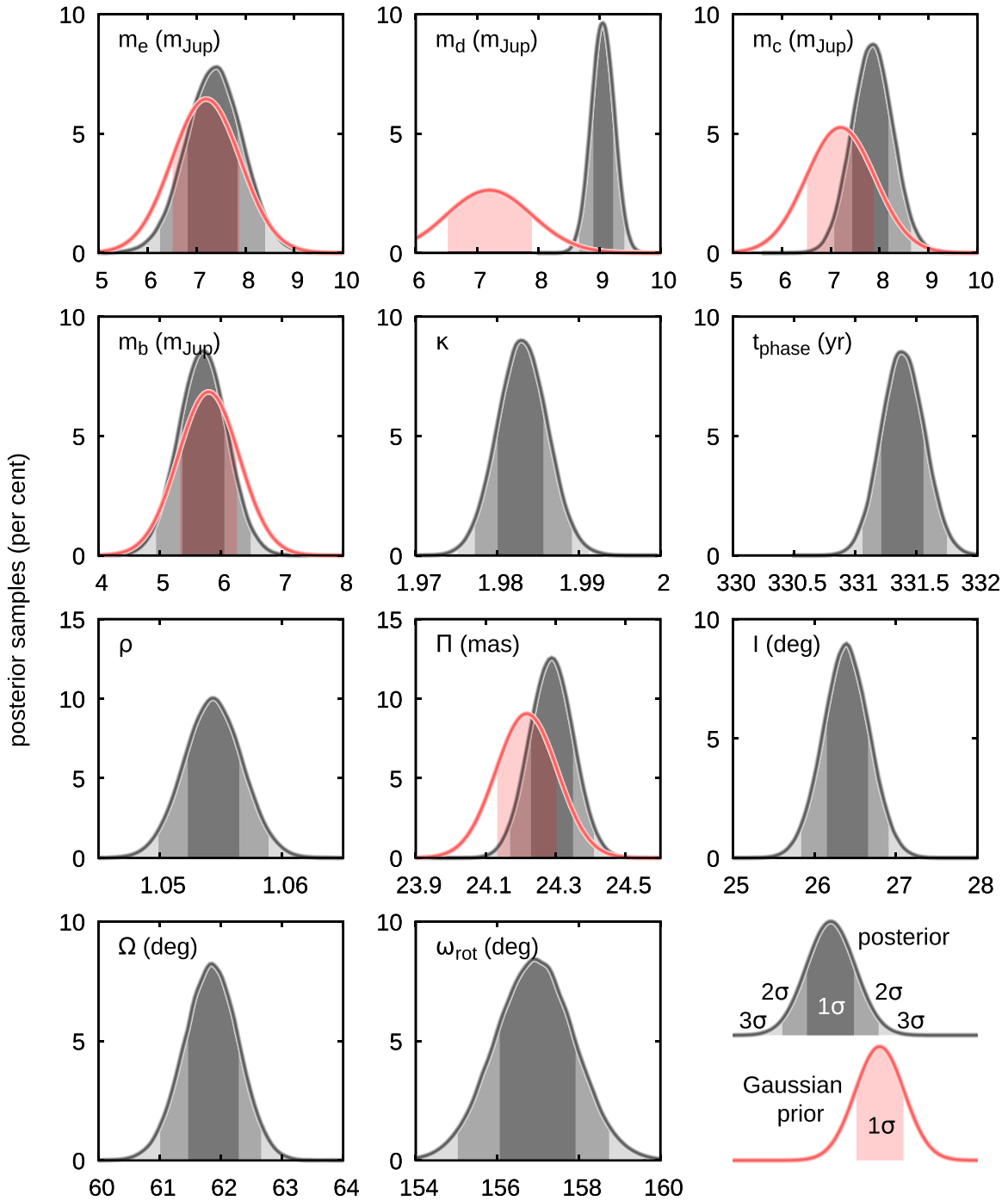
Figure A5. Posterior probability distributions for the free parameters of the PO model of the HR 8799 system (gray curves). The shades of gray are for 1σ, 2σ, and 3σ confidence intervals. Red curves mark the Gaussian priors set for five out of 11 model parameters. The red areas under the curves indicate 1σ ranges of each parameter. The remaining six parameters of the model have the uniform (noninformative) priors, not shown in the plot. See Table 1 and the text in Appendix A.

particular, the bottom right panel in Figure 3 (also Figure A5) illustrates the Gaussian prior as a Gaia parallax (Gaia Collaboration et al. 2018; red curve) overplotted with the DE-MC posterior. The distributions closely overlap. We also recall the grid-based experiments indicating that the best-fitting parallax may be determined independently of the Gaia measurements. The one-dimensional posterior probability distributions of all of the free parameters determined with the DE-MC sampling are shown in Figure A5, while two-dimensional contour plots of the posteriors for the Keplerian elements are illustrated in Figure A6. The parameter uncertainties derived from the sampling are listed in Table 1. The dynamical analysis of this solution in terms of the orbital evolution and stability is illustrated in Figures A7 and A8.
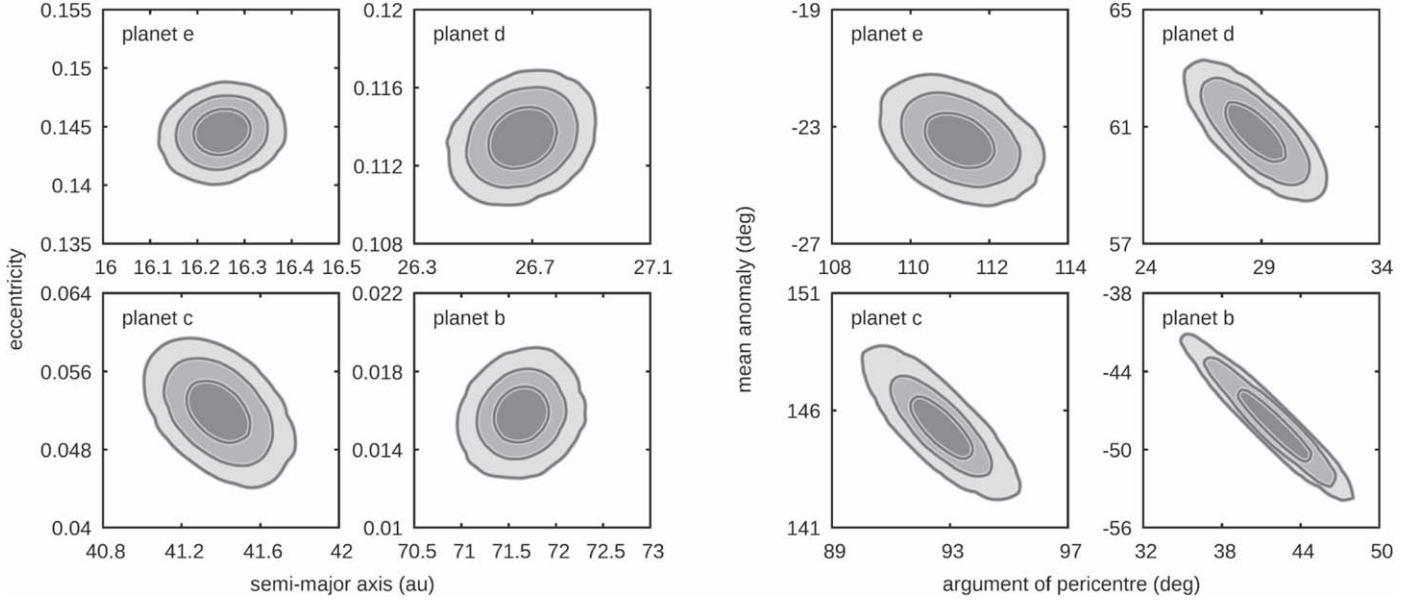
Figure A6. Posterior probability distributions presented in diagrams of semimajor axis vs. eccentricity (left four panels), as well as the argument of pericenter vs. the mean anomaly (right four panels). The shades of gray, from darkest to lightest, represent 1σ, 2σ, and 3σ confidence levels.
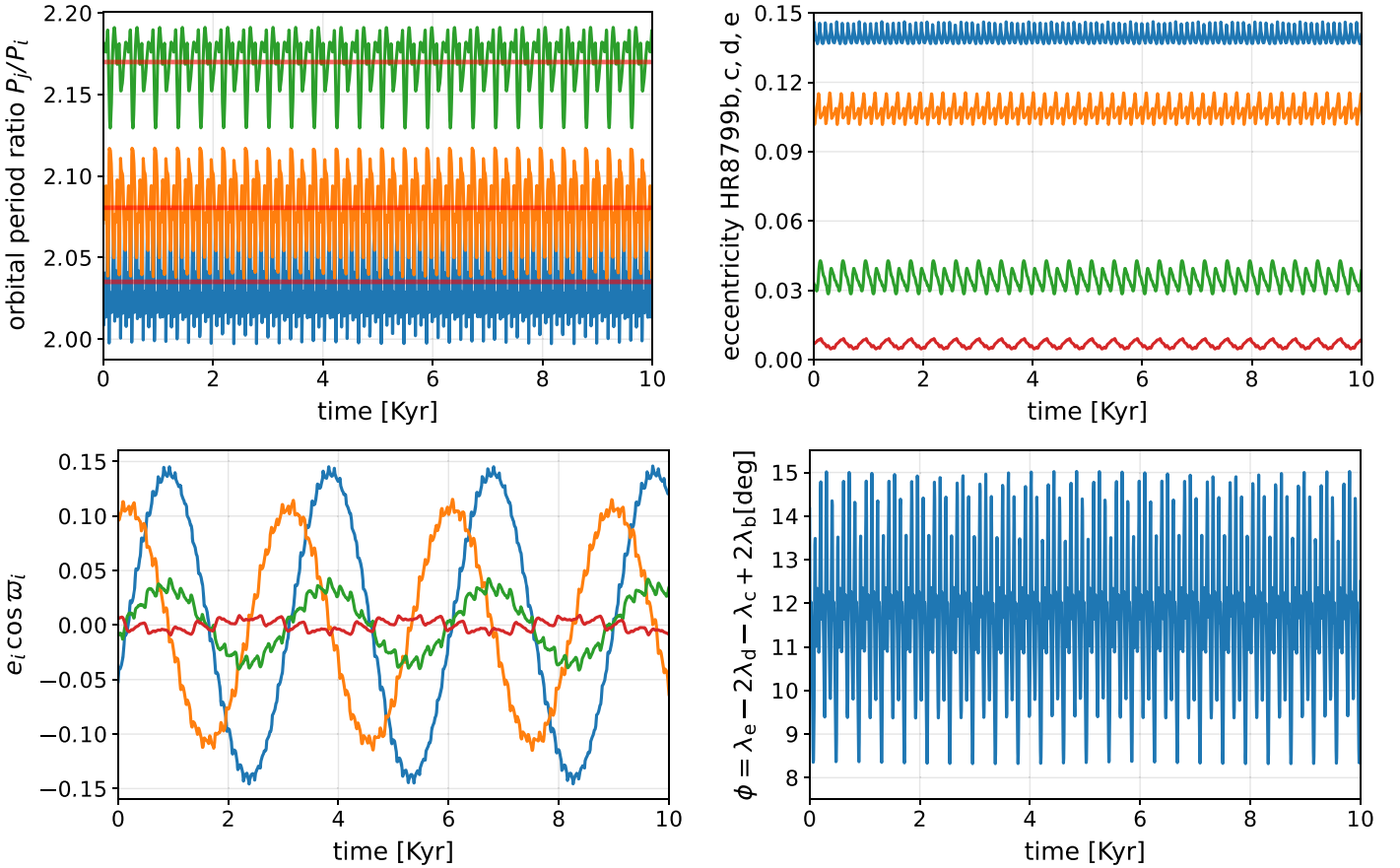

Figure A7. Temporal evolution, for the first 10 Kyr, of the canonical, osculating orbital elements, expressed in the Jacobian reference frame, for the PO configuration in Table 1. Top left panel: osculating period ratios for a subsequent pair of planets and their mean values (horizontal red lines), from top to bottom, $P_b/P_c \simeq 2.170$, $P_c/P_d \simeq 2.081$, and $P_d/P_e \simeq 2.035$. We note that the proper orbital periods, in the sense of the mean motions as fundamental frequencies (Morbidelli 2002) expressed in Julian years of 365.25 days, are 52.36995, 104.73989, 209.47987, and 418.96324 for planets HR 8799e, d, c, and b, respectively, forming an exact 2:1, 2:1, 2:1 MMR chain. Top right panel: eccentricities of the planets HR 8799e, d, c, and b from top to bottom. Bottom left panel: one of the elements $x_i \equiv e_i \cos \varpi_i$ (i = HR 8799b, c, d, and e) used to compute the secular frequency of the apsides rotation. The second component of the quasiperiodic signal (not shown) is $y_i \equiv e_i \sin \varpi_i$. Bottom right panel: critical argument of the zeroth-order, four-body generalized Laplace resonance for the same initial condition that librates around $\simeq 12°$.
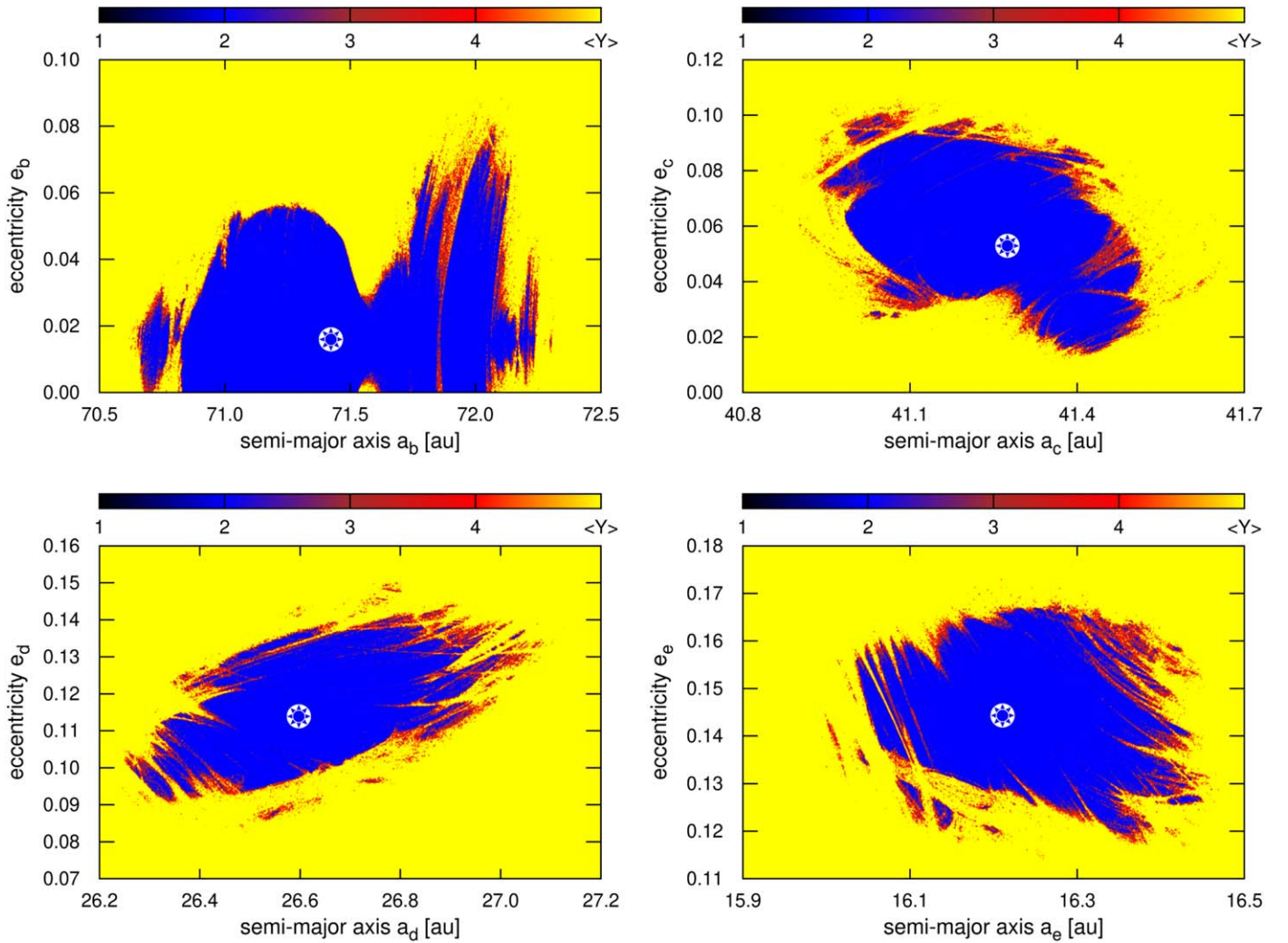
Figure A8. Dynamical maps in the semimajor axis–eccentricity plane in terms of the MEGNO fast indicator. Each point in the maps was integrated for 10 Myr, equivalent to more than 20,000 orbits of planet HR 8799b. Stable systems are confined to $\langle Y \rangle \simeq 2$ (blue), and yellow marks strongly unstable configurations that are typically self-disrupting in less than 1 Myr. The star symbols mark the nominal osculating elements in the initial condition in Table 1 for each planet in subsequent panels. The resolution of each map is 800×480 pixels.

Appendix B
Masses with Regard to Data Biases

With the improved PO algorithm described in Appendix A.3, we systematically explored the χ^2 minimum in two-dimensional planet mass planes, without (Figure B1) and with independently determined astrophysical priors (Figure B2), regarding the measurement set $\mathcal{D}$ with $N_{\rm obs} = 65$ observations and also reducing it by particular GPI points (hereafter data set $\mathcal{D}_1$), as explained below. For a given fixed point in a selected two-dimensional mass plane, the remaining two masses and the κ period ratio are optimized in terms of the best-fitting χ^2. In the χ^2 optimization, the mass priors may be included as additional terms in the χ^2 function (Equation (A3)): $(m_i - m_{i,{\rm cooling}})^2/(\sigma_{i,{\rm cooling}})^2$, where $i =$ e, d, c, and b and $m_{i,{\rm cooling}}$ denotes the planet i mass constraint (prior), while $\sigma_{i,{\rm cooling}}$ is its 1σ uncertainty. We set the mass priors after Wang et al. (2018), the same as in the DE-MC experiments. The χ^2 scans in the mass planes for this enhanced model are shown in Figure B2. We note that in the χ^2 experiments, the parallax was treated as a free parameter with no prior.

In the first experiment for data set $\mathcal{D}$ and without considering mass priors, we found the best-fitting $m_{\rm e} \lesssim 0.1 m_{\rm Jup}$. Also, the best-fitting and astrophysical masses are significantly different, as marked in the top row of Figure B1, particularly for HR 8799d. In this figure, the mass estimates from the cooling theory are shown for reference. The masses of HR 8799e and HR 8799c are strongly anticorrelated and not bounded at all, since the best-fitting $m_{\rm e}$ converges toward very small and nonrealistic values. When fixing the inner planet's mass at $7\,m_{\rm Jup}$, the anticorrelation disappears, and masses $m_{\rm d}$ and $m_{\rm b}$ become much better constrained, but their values are still significantly shifted with respect to the astrophysical priors (Figure B2, top row).

In order to explain the discrepancy between the prior and posterior estimates, especially significant for the mass of HR 8799d and also revealed by the MCMC sampling, we searched for possible data biases. The left panel of Figure B3 illustrates the R.A. and decl. residuals of the best-fitting model in Table 1 derived for the $\mathcal{D}$ set; rows from top to bottom are for subsequent planets. While the most precise GRAVITY datum is modeled apparently perfectly, there are precision GPI
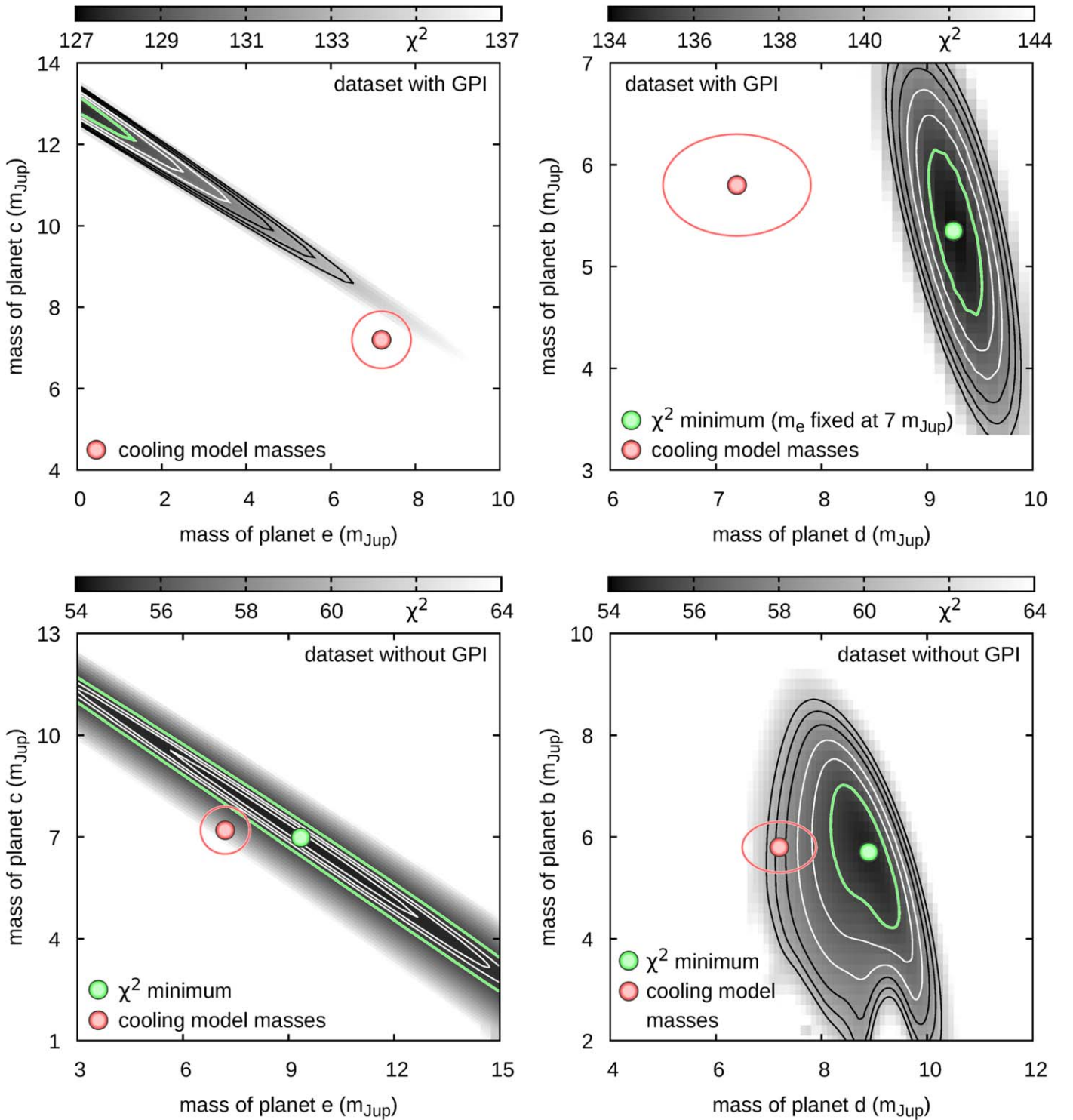
Figure B1. A χ^2 scan of PO models in the plane of masses HR 8799e and HR 8799c (left panels) and HR 8799d and HR 8799b (right panels) for the data set with (top row; $\mathcal{D}$) and without (bottom row; $\mathcal{D}_1$) the GPI measurements. The red filled symbols and circles/ellipses reference astrophysical masses $m_e = (7.2 \pm 0.7)m_{Jup}$ and $m_c = (7.2 \pm 0.7)m_{Jup}$ (left panels) and $m_d = (7.2 \pm 0.7)m_{Jup}$ and $m_b = (5.8 \pm 0.5)m_{Jup}$ (right panels) following Wang et al. (2018). The green filled point denotes the position of the minimum of χ^2 function, while the green contour denotes the level of min $\chi^2 + 1$. The white and black curves denote the levels of min $\chi^2 + 2$, ..., $+6$, apart from the bottom left panel, in which the white contours denote the confidence levels of min $\chi^2 + 0.1$, $+0.3$, $+0.5$.

observations (Wang et al. 2018) significantly deviating from the astrometric model, compared to the uncertainties. In the next experiment, we temporarily removed these points from the data set, and we found a new best-fitting model for this modified set $\mathcal{D}_1$, with residuals shown in the right panel of Figure B3. The GPI points, overplotted with bigger gray

symbols, reveal systematic shifts with regard to this best-fitting model.

Figure B4 illustrates the residuals in the (R.A., decl.) plane. All of the GPI points exhibit a systematic positive R.A. shift with respect to the model, and apart from one point, all of them have negative decl. deviations (top left panel). Moreover, most
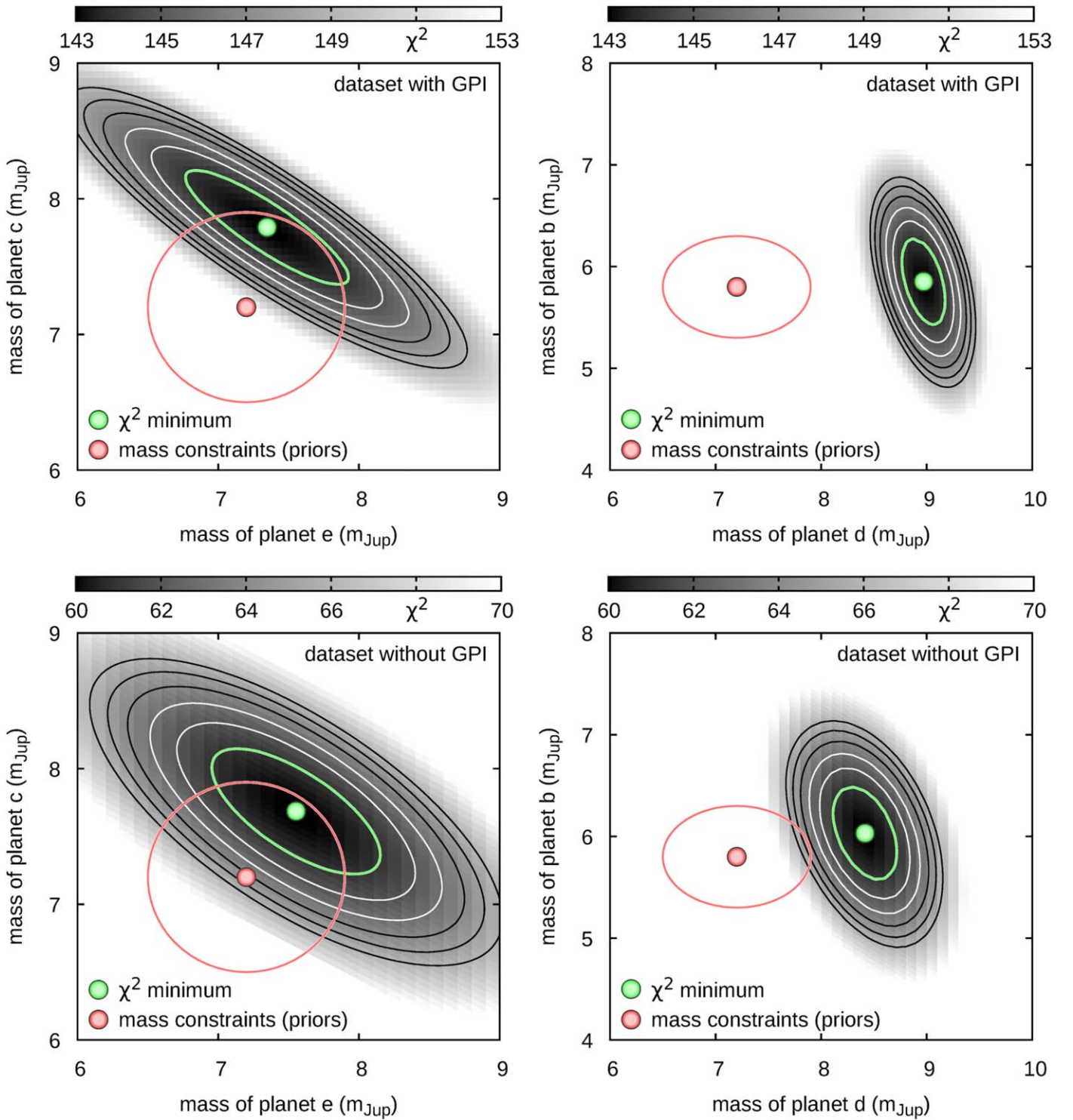
Figure B2. A χ^2 scan of PO models in the mass plane of HR 8799e and HR 8799c (left panels) and HR 8799d and HR 8799b (right panels) for the data set with (top row; $\mathcal{D}$) and without (bottom row; $\mathcal{D}_1$) the GPI measurements, as well as with the hot-start cooling theory priors. The red filled symbols and circles/ellipses correspond to $m_e = (7.2 \pm 0.7)m_{Jup}$ and $m_c = (7.2 \pm 0.7)m_{Jup}$ (left panels) and $m_d = (7.2 \pm 0.7)m_{Jup}$ and $m_b = (5.8 \pm 0.5)m_{Jup}$ (right panels) following Wang et al. (2018). The green filled point denotes the position of the minimum of χ^2 function, while the green contour denotes the level of min $\chi^2 + 1$. The white and black curves denote the confidence levels of min $\chi^2 + 2$, ..., $+ 6$.

of the data points deviate from the model by more than 3σ (bottom left panel in Figure B4). Observations $\mathcal{D}_1$, without the GPI data, are distributed uniformly in the (R.A., decl.)–residuals plane, as expected for a statistically valid solution (right column). This may suggest a bias in the GPI data with

regard to the other measurements, yet the bias is of an unknown origin.

The obtained χ^2 minima with mass priors for data set $\mathcal{D}$, presented in the top row of Figure B2, overlap with the results of the DE-MC sampling around the best-fitting model
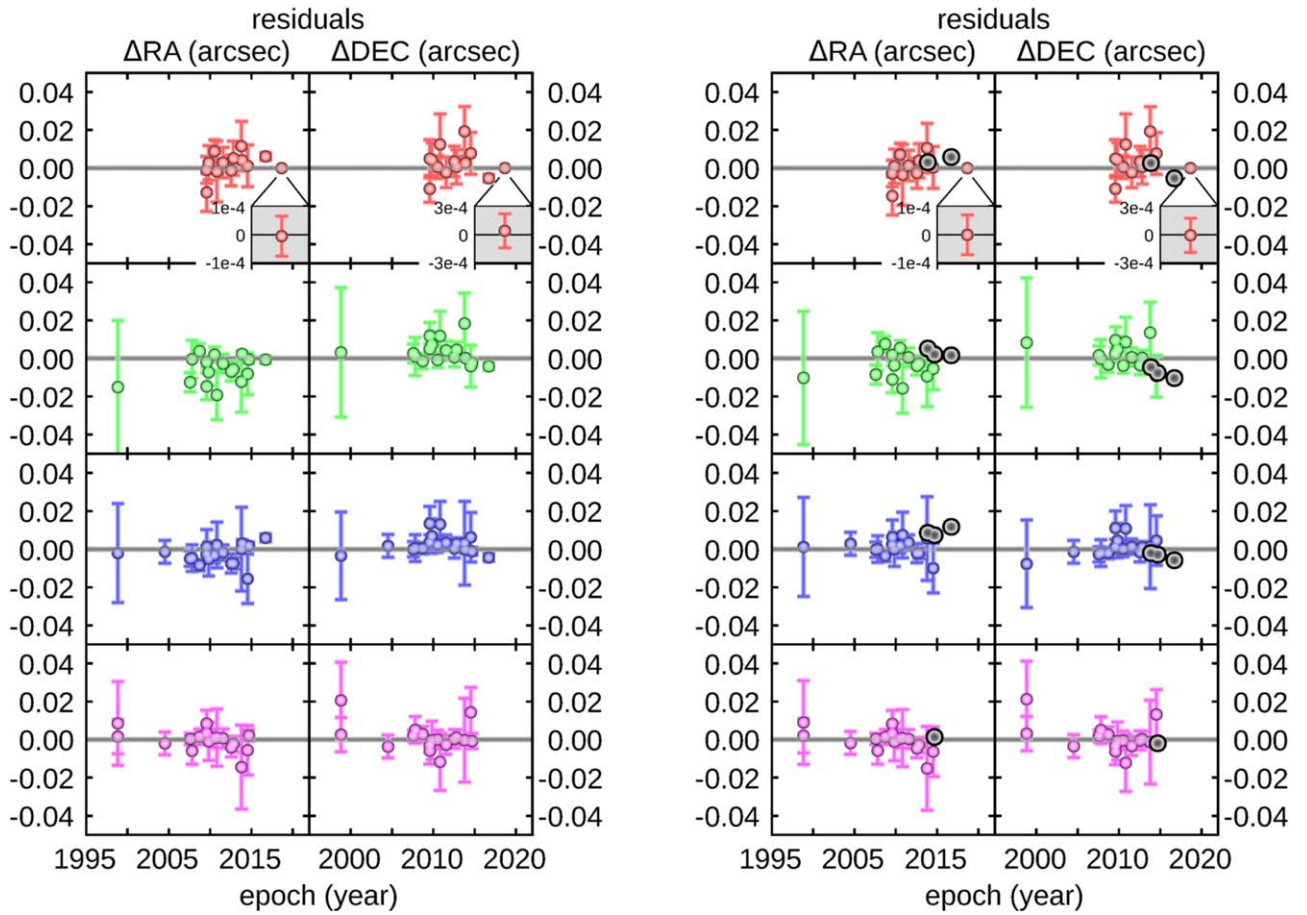
Figure B3. Residuals of the best-fitting model to the data set with (left panel; $\mathcal{D}$) and without (right panel; $\mathcal{D}_1$) the GPI observations. In the right panel, the GPI data not included in the fitted data set are marked with big gray symbols without error bars. The GRAVITY datum for HR 8799e is additionally enlarged in the top row (gray rectangles).

illustrated in Figures A5 and A6. As noted above, the best-fitting mass of planet HR 8799d is the only one significantly inconsistent with the priors from thermodynamical tracks by $\simeq 2\,m_{\rm Jup}$ (top row of Figure B2). However, when the GPI measurements are excluded from the data set, the difference reduces by factor of $\simeq 2$, making the astrometric model results marginally consistent with the HR 8799d mass determined from the cooling theory (bottom row of Figure B2). All masses

become constrained much better for the reduced data set $\mathcal{D}_1$ than $\mathcal{D}$ and are marginally consistent with the astrophysical values, although their uncertainties are still significant. This experiment demonstrates the sensitivity of the astrometric model to the most accurate data points. We also recall that, with just one added GRAVITY-like measurement for each planet close to the present epoch, the astrometric data alone might fully constrain the masses (see the main text and Figure 5).
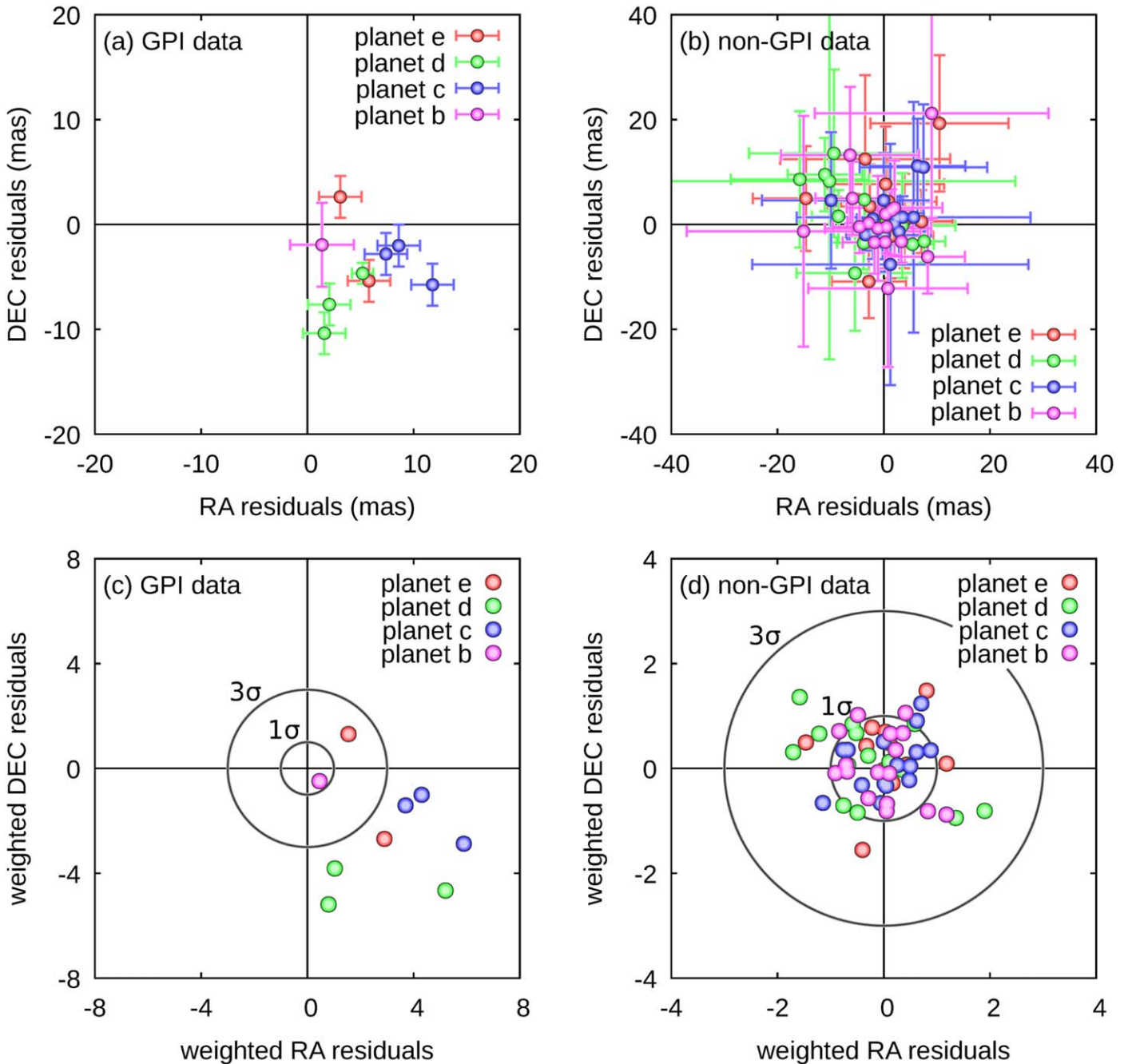
Figure B4. Residuals of the best-fitting model without the mass priors and GPI data. The top panels show the residuals together with their uncertainties, while the bottom panels show the residuals weighted with the uncertainties. Circles of radii equal to 1 and 3 mark 1σ and 3σ deviations of a given data point from the model. In the right panels, the fitted astrometric measurements are illustrated. Deviations of the GPI data from the model are presented in the left panels.

Appendix C
The Debris Disk Simulation

C.1. The N-body Model of the Debris Disks

Given the ongoing discussion in the literature, as summarized in the main text, we aim to resolve the dynamical structure of the debris disks composed of small Kuiper Belt–like objects. Such a structure may reflect unique characteristics implied by the strictly resonant motion of the planets. Here we essentially follow the approach in GM18. The numerical model relies on determining the orbital stability of small-mass particles in the HR 8799 system through resolving the chaotic or regular character of their motion with the MEGNO $\langle Y \rangle$ fast indicator

(Cincotta et al. 2003). We dubbed it the $\langle Y \rangle$-model. As we found in GM18 with the long-term, direct N-body integrations, the $\langle Y \rangle$-model closely reproduces the dynamical structure of the debris disks found with the direct integrations but in a much shorter computation time.

Here we conducted an extensive $\langle Y \rangle$-model simulation of the debris disks coplanar with the planets involved in the exact Laplace resonance (Table 1). We considered three mixed fractions of asteroids with masses of $10^{-15}\,m_{\rm Jup}$, similar to GM18, as well as 10^{-10} and $10^{-6}\,m_{\rm Jup}$. As the initial Keplerian osculating elements, we randomly draw the semimajor axis $a_0 \in [10,\,400]$ au, the pericenter longitude, and the mean anomaly $\varpi_0,\,\mathcal{M}_0 \in [0°,\,360°)$. For the inner part of the disk
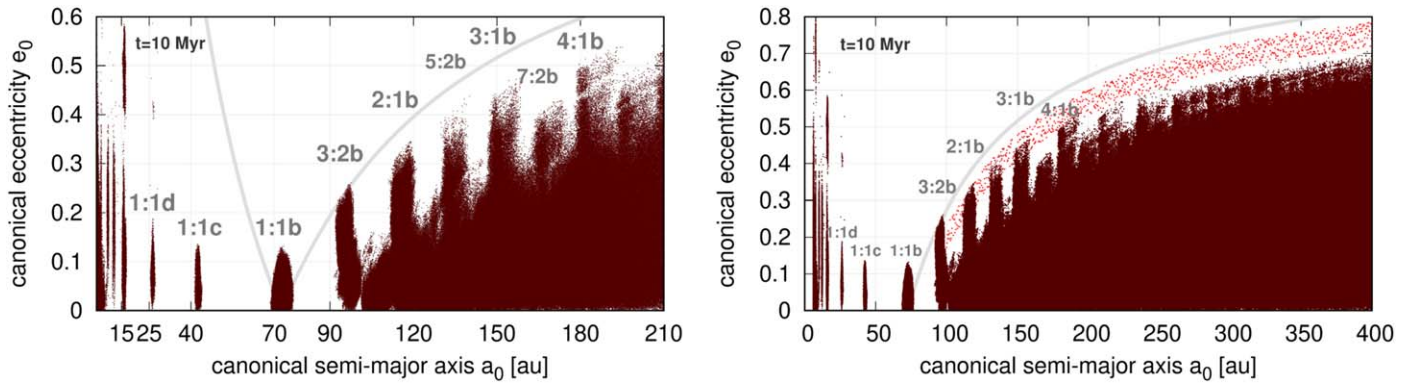
Figure C1. Canonical Poincaré elements (a_0, e_0) of $\langle Y \rangle$-stable solutions at the end of the integration interval of 10 Myr. Gray lines are for the collision curve of orbits with planet HR 8799b. Approximate positions of a few low-order MMRs with planets HR 8799b and HR 8799c are labeled. The left panel is for the inner part of the disk, and the right panel is for the whole simulation. Red filled circles in the right panel illustrate 1000 initial conditions of test orbits, analyzed in order to explain the wide instability zone below the collision curve.

($a_0 < 100$ au), we selected $e_0 \in [0, 0.9]$, and for the outer part, beyond planet HR 8799b, $e_0 < 1 - (a_0/a_b)(1 + e_b)$, i.e., under the collision curve of asteroids with HR 8799b in the (a_0, e_0)-plane. We integrated the equations of motion and the variational equations for the whole N-body system of the observed planets (Table 1, primaries), updated by a test particle, with the Bulirsh–Stoer–Gragg (BGS) integrator. The local and absolute accuracy of the integrator set to $\epsilon = 10^{-13}$ provided a relative energy error as small as 10^{-9} for the total integration time of 10 Myr. The BGS algorithm has been proven reliable for collisional and chaotic dynamics, which may be anticipated on the basis of previous works (GM18).

Concerning the appropriate integration time required to reliably characterize the orbits of asteroids, we note that the four massive planets are locked deeply in the Laplace resonance (Figure A7), and each planet is located in the center of the stability zone (Figure A8). The system stability is robust to perturbations of quite massive additional companions (see also simulations in GM18 for "asteroid" masses as large as 1–2 m_{Jup}). Therefore, the $\langle Y \rangle$ integrations of the best-fitting initial condition extended by the elements of a test asteroid reveal the dynamical character of its motion, and the orbits of the primaries are not affected.

The geometric structure of the debris disks is illustrated in Figures 4, C1 and C2. In the numerical experiment, we collected $\simeq 3.3 \times 10^6$ $\langle Y \rangle$-stable orbits. The astrocentric positions of the asteroids are marked at the end of the integration time (top left panel of Figure C2) and at the initial epoch (top right panel of Figure C2) and color-coded according to their osculating eccentricity. Such snapshots represent a population of quasiperiodic and resonant orbits of the asteroids with various orbital phases and eccentricity, while their semimajor axes may overlap. We note, following GM18, that the orbits might be potentially present in the real system, but the actual population of asteroids may depend on the formation history of the whole system, its migration history, and a locally variable density of asteroids.

In regions interior to and beyond the orbit of planet HR 8799b, the majority of the test orbits are extremely chaotic, except of particular resonant solutions. Such $\langle Y \rangle$-unstable orbits are also strongly unstable in the Lagrangian (geometric) sense; particles are ejected or collide with the primaries on a timescale of a few Myr only. We found this after testing the semimajor axis–eccentricity evolution in time for orbits selected in a strip

of 1000 initial conditions marked with red filled points in the right panel of Figure C1. It shows the proper (canonical) elements (Morbidelli 2002) of dynamically stable asteroids in the semimajor axis–eccentricity plane (a_0, e_0); see the right panel. In order to study unstable motions, test particles were randomly placed under the collision curve with planet HR 8799b. The initial eccentricity of their orbits is slightly larger than the respective limit of $\langle Y \rangle$-stable motions, and the initial semimajor axes $a_0 \in [100, 400]$ au, as well as initial phases, are also random. We closely investigated the orbits of all of these test asteroids by integrating them for 10 Myr. In this set, 466 asteroids collided with planet HR 8799b, 128 objects collided with the star, and 351 asteroids were ejected from the system beyond 5000 au, leaving the radius of 800 au typically in a few Myr and less than the maximum interval of 10 Myr. Only $\simeq 50$ objects located in stable, resonant regions survived for the maximum integration interval.

Moreover, with the modified Fourier transform or fundamental frequency analysis (Šidlichovský & Nesvorný 1996) of the canonical Jacobi elements $z_i = e_i(\cos \varpi_i + \sqrt{-1} \sin \varpi_i)$, ($i = $ b, c, d, e), illustrated in the bottom left panel in Figure A7, we computed the frequency spectrum of planet pericenter rotation $\dot{\varpi}(t)$. Since the motion of the planets is strictly periodic, the $z_i(t)$ signals involve a common leading frequency $f_\varpi = -440\overset{''}{.}418 \, \mathrm{yr}^{-1}$, equivalent to the retrograde rotation of the system with a period $P_\varpi \simeq 2942.66$ yr, i.e., only $\simeq$ six orbits of planet HR 8799b. Besides the leading frequency, there are a few even larger, with periods smaller than 1000 yr.

Since the dynamics is governed by short-term MMRs and, possibly, secular resonances, we could fix the same integration time of 10 Myr across the whole disk. That integration time corresponds to $\simeq 20,000$ orbital periods of the outermost planet and roughly 12,000 orbits at $\simeq 100$ au, which is sufficient to resolve the dynamical character of asteroid orbits. Particles marked as $\langle Y \rangle$-stable for that interval of time should persist for a more than 10 times longer interval in Lagrange-stable orbits, roughly 100–160 Myr (see GM14; GM18), which is much longer than typical estimates of the parent star lifetime, $\simeq 42$ Myr (Wang et al. 2018), in the 30–60 Myr range earlier adopted in Marois et al. (2010). At the outer edge of the disk, $\simeq 430$ au, as determined by Booth et al. (2016), the integration interval translates to a few thousand orbital periods, which is still meaningful to determine the stability border in the (a_0, e_0)-plane, as we justified above. Moreover, given the strong
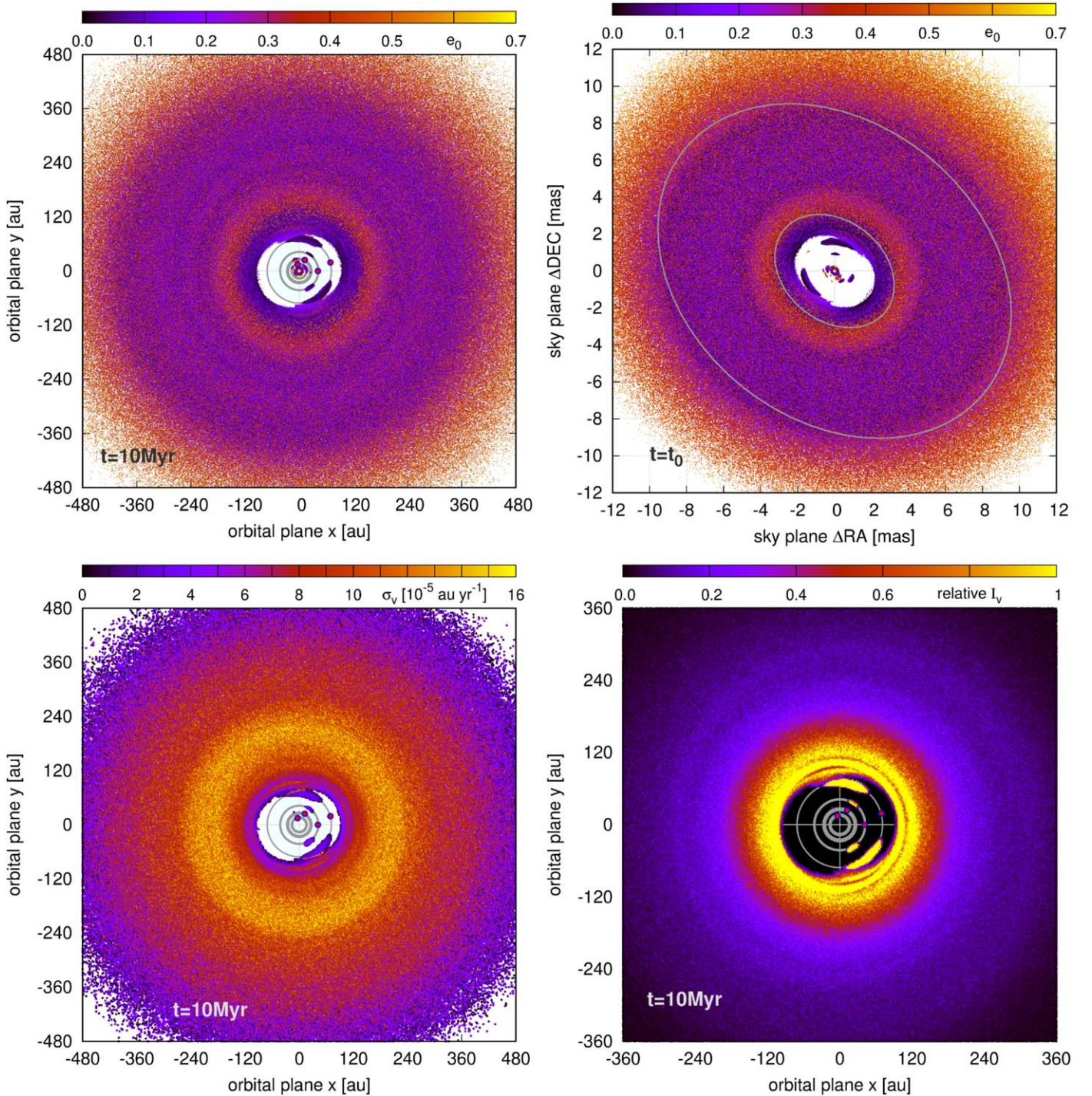
Figure C2. Top left panel: global view of the debris disk revealed by $\simeq 3.3 \times 10^6 \langle Y \rangle$-stable orbits of the whole simulation illustrated as a snapshot of the astrocentric coordinates (x, y) of the asteroids at the end of the integration interval of 10 Myr. The osculating orbital eccentricities e_0 of these orbits are color-coded and labeled in the top bar. The initial positions of the planets are marked with filled circles. Gray rings illustrate their orbits integrated for 10 Myr. Top right panel: similar to Figure 4 and the top left panel, but the initial astrocentric (x, y)-coordinates of asteroids in $\langle Y \rangle$-stable orbits are rotated by the inclination and nodal angles of the initial condition in Table 1. Gray ellipses illustrate the disk boundaries $r_{\rm in} = 145$ au and $r_{\rm out} = 429$ au fitted in Booth et al. (2016) and rotated by inclination $I = 41°$ and nodal angle $\Omega = 50°$ derived in this paper. Bottom left panel: velocity dispersion in the debris disks evaluated at 2 au $\times$ 2 au bins and color-coded over the initial astrocentric (x,y)-coordinates of asteroids in $\langle Y \rangle$-stable orbits. Bottom right panel: relative Planck intensity of the outer disk, $I_\nu \sim K\Sigma(r)r^{-1/2}$, as in Read et al. (2018), where $\Sigma(r)$ is proportional to the number of asteroids in 2 au $\times$ 2 au bins, the same as calculated in the velocity dispersion plot in the bottom left panel.

instability generated by the short-term interactions, the $\langle Y \rangle$ integrations may be stopped as soon as $\langle Y \rangle > 5$, sufficiently different from $\langle Y \rangle \simeq 2$ for stable systems. That makes it possible to examine large sets of a few 10^7 test orbits, orders of

magnitude larger than they could be sampled with the direct N-body integrations. The most complex and interesting parts of the debris disks may then be mapped in detail with the $\langle Y \rangle$-model.

Regarding the inner part of the system, we found the same irregular inner boundary of the outer disk, similar to simulations in GM18. In order to understand this feature, we analyze the (a_0, e_0) diagram, shown in Figure C1. Comparing the left panel of Figure C1 with the disk structure illustrated in Figure 4, we find that the inner edge of the outer disk is significantly asymmetric due to low- and moderate-eccentricity orbits in the 1:1 and 3:2 MMR with planet HR 8799b. The low density of asteroids around $\simeq 110$ au appears due to an unstable 2:1 MMR and higher-order resonances forming a kind of thickening "comb" with increasing semimajor axis. It forms a border of stable orbits shifted below the collision curve with planet HR 8799b by a substantial value of ~ 0.1. We can now understand and interpret the strongly unstable orbital evolution of the tested asteroids in this zone (Figure C1, right panel). The strong instability is caused by overlapping two-body MMRs, multibody MMRs, and (possibly) mixed secular MMRs. The pericenter frequency of the system is commensurate with the mean motion of asteroids n_0 in this zone; for instance, regarding absolute values of the frequencies, $1f_\varpi : 1n_0$ at $\simeq 235$ au, $3f_\varpi : 2n_0$ at $\simeq 310$ au, $2f_\varpi : 1n_0$ at $\simeq 375$ au, and $3f_\varpi : 1n_0$ at $\simeq 490$ au. However, the resonances are retrograde for the disk rotating with the same spin direction as the planets; therefore, we did not observe their direct or clear dynamical influence on the asteroids. A streaking feature of the stable zone beyond HR 8799b is the presence of low-density rings, which could be identified with higher-order resonances with this outermost planet, such as 2:1, 3:2, 3:1, and 5:2, extending up to $\simeq 200$ au (Figures C1 and 4).

A stable 1:1 MMR with planet HR 8799b forms huge, symmetric Lagrangian areas of low-eccentricity objects extending for 70–80 au and $\simeq 10$ au across. The Lagrangian 1:1 MMRs governed by inner planets are nonsymmetric in respective pairs. There are also islands of the 2:1 and 3:2 MMRs with HR 8799d and HR 8799e. In these islands, the eccentricity of the asteroids reaches $e_0 \simeq 0.8$ (yellow in Figure 4). The outer continuous edge of the inner debris disk appears at $\simeq 8$ au. (The dynamical structure of the inner disk was investigated in more detail in GM18.)

In the top panels of Figure C2, we present the global view of the debris disks revealed by $\simeq 3.3 \times 10^6 \langle Y \rangle$-stable orbits in the whole simulation. Similarly to Figure 4, the panels represent snapshots of the astrocentric coordinates (x, y) of the asteroids and their osculating orbital eccentricities e_0 (color-coded and labeled in the top bar) at the initial epoch (right panel) and at the end of the integration interval of 10 Myr (left panel). We selected the end epoch in order to illustrate a saturation of asteroids after a substantial interval of thousands of orbital periods. The initial positions of the planets are marked with filled circles. For reference, gray rings illustrate their orbits integrated for the same interval of 10 Myr, with the initial conditions in Table 1, independently of the disk integrations.

The top left panel of Figure C2 shows the debris disks in the orbital plane at the final epoch $t = 10$ Myr, and the top right panel is for the sky view of the disks at the initial epoch t_0, rotated by the inclination and nodal angle in the initial condition (Table 1). These global representations for the outer disk reveal a ring of highly eccentric orbits between $\simeq 140$ and $\simeq 200$ au and a broad outer ring forming a diffuse outer edge of the disk. We note that the inner ring is substantially shifted with respect to the inner edge of the disk found at $\simeq 90$ au. The

dynamical structure of the whole disk is also illustrated in the (a_0, e_0)-plane of the canonical Poincaré elements in the right panel of Figure C1. In the top right panel of Figure C2, we also marked the inner and outer boundary of the disk model in Booth et al. (2016), according to their estimate of the inclination $I = 41°$ and nodal angle $\Omega = 50°$. These values appear substantially different from the inclination and nodal angle of the best-fitting elements of the planetary system orbital plane (Table 1).

In order to interpret the ring structure around $\simeq 150$ au, we plotted (not shown here) the canonical osculating eccentricity e_0 versus the astrocentric radius of particles at the epoch t_0, and also at $t_0 + 10$ Myr. They reveal that the excess of particles with high eccentricity seems to be a real feature, unlikely to be due to a particular sampling or plotting order of the particles. It is also clear that e_0 is a very steep function of the radius r_0 at the innermost part of the outer disk.

Given the variation of eccentricity across the disk, we computed the Keplerian velocity dispersion of the particles. We binned asteroids in the region covering the whole disk, $x, y \in [-480, 480]$ au in square bins of 2 au × 2 au. In each box with a nonzero number of particles, we computed $\sigma_v^2 = \sum_i^n (v_i - \bar{v})^2 / n$, where v_i is the velocity module of a particle i in the given bin, n is the counted number of particles in this bin, and $\bar{v}$ is the mean velocity module. The results are illustrated in the bottom left panel of Figure C2. The ring structure associated with high-eccentricity asteroids and the gradient of $e_0(r_0)$ implies a velocity dispersion σ_v a few times larger than in the inner parts of the disk. It could imply more intense dust production due to both a locally larger density of objects and higher velocity during their collisions. We may note that the inner disk boundary fitted by Booth et al. (2016) seems to overlap with the eccentricity ring edge, which could suggest a systematic shift of the detected emission with regard to the actual dynamical border of the disk at $\simeq 100$ au. It might actually confirm the results of Wilner et al. (2018) in their more recent model of the disk also predicting the inner edge at $\simeq 100$ au. Such a border is more consistent with our updated orbital model of the HR 8799 system regarding the present parallax estimate in the Gaia DR2 catalog and the resulting true linear dimensions of the system.

Finally, we simulated the relative intensity image of the disk. The relative intensity is defined the same as in Read et al. (2018), $I_{\nu(r)} \sim K \Sigma(r) r^{-1/2}$, where $\Sigma(r)$ is the surface density and K is the scaling factor. In order to estimate $\Sigma(r)$, we used the counts of asteroids in the same 2 × 2 au bins used for computing the velocity dispersion. The results are illustrated in the bottom right panel of Figure C2. The bright rings are associated with fractions of stable asteroids in the 3:2 and 2:1 MMRs with planet HR 8799b.

While interpretation of the results needs more work, we might briefly conclude that the disk simulation reveals features related to the resonant character of the system. They consist of asymmetry of the inner edge of the outer debris disk and a highly variable density of asteroids in its inner part due to low-order MMRs with planet HR 8799b, including large Lagrangian clouds. There are also two possible rings of high-eccentricity asteroids around 140–160 au and at the outer edge $\simeq 430$ au. These features may influence the intensity images used for modeling the emission in different wavelengths, and they should likely be accounted for in order to avoid biases in the emission models.

ORCID iDs

Krzysztof Goździewski ● https://orcid.org/0000-0002-8705-1577
Cezary Migaszewski ● https://orcid.org/0000-0003-2546-6328

References

Beaugé, C., Michtchenko, T. A., & Ferraz-Mello, S. 2006, MNRAS, 365, 1160
Bergfors, C., Brandner, W., Janson, M., Köhler, R., & Henning, T. 2011, A&A, 528, A134
Booth, M., Jordán, A., Casassus, S., et al. 2016, MNRAS, 460, L10
Broer, H., & Hanßmann, H. 2016, Indagationes Math., 27, 1305
Cincotta, P. M., Giordano, C. M., & Simó, C. 2003, PhyD, 182, 151
Currie, T., Burrows, A., Girard, J. H., et al. 2014, ApJ, 795, 133
Currie, T., Burrows, A., Itoh, Y., et al. 2011, ApJ, 729, 128
Currie, T., Fukagawa, M., Thalmann, C., Matsumura, S., & Plavchan, P. 2012, ApJL, 755, L34
De Rosa, R. J., Nguyen, M. M., Chilcote, J., et al. 2020, JATIS, 6, 015006
Delisle, J. B. 2017, A&A, 605, A96
Esposito, S., Mesa, D., Skemer, A., et al. 2013, A&A, 549, A52
Fabrycky, D. C., Lissauer, J. J., Ragozzine, D., et al. 2014, ApJ, 790, 146
Gaia Collaboration, Brown, A. G. A., Vallenari, A., et al. 2018, A&A, 616, A1
Galicher, R., Marois, C., Macintosh, B., Barman, T., & Konopacky, Q. 2011, ApJL, 739, L41
Geiler, F., Krivov, A. V., Booth, M., & Löhne, T. 2019, MNRAS, 483, 332
Götberg, Y., Davies, M. B., Mustill, A. J., Johansen, A., & Church, R. P. 2016, A&A, 592, A147
Goździewski, K., & Migaszewski, C. 2014, MNRAS, 440, 3140
Goździewski, K., & Migaszewski, C. 2018, ApJS, 238, 6
GRAVITY Collaboration, Lacour, S., Nowak, M., et al. 2019, A&A, 623, L11
Gregory, P. 2010, Bayesian Logical Data Analysis for the Physical Sciences (Cambridge: Cambridge Univ. Press)
Hadjidemetriou, J. D. 1976, Ap&SS, 40, 201
Hadjidemetriou, J. D., & Michalodimitrakis, M. 1981, A&A, 93, 204
Henry, G. W., Marcy, G. W., Butler, R. P., & Vogt, S. S. 2000, ApJL, 529, L41
Hinz, P. M., Rodigas, T. J., Kenworthy, M. A., et al. 2010, ApJ, 716, 417
Ida, S., Tanaka, H., Johansen, A., Kanagawa, K. D., & Tanigawa, T. 2018, ApJ, 864, 77

Izzo, D., Ruciński, M., & Biscani, F. 2012, in Parallel Architectures and Bioinspired Algorithms, Studies in Computational Intelligence, Vol. 415, ed. F. Fernández de Vega, J. Hidalgo Pérez, & J. Lanchares (Berlin: Springer), 151
Johansen, A., & Lambrechts, M. 2017, AREPS, 45, 359
Konopacky, Q. M., Marois, C., Macintosh, B. A., et al. 2016, AJ, 152, 28
Lafrenière, D., Marois, C., Doyon, R., & Barman, T. 2009, ApJL, 694, L148
Lithwick, Y., Xie, J., & Wu, Y. 2012, ApJ, 761, 122
Maire, A.-L., Skemer, A. J., Hinz, P. M., et al. 2015, A&A, 576, A133
Marois, C., Macintosh, B., Barman, T., et al. 2008, Sci, 322, 1348
Marois, C., Zuckerman, B., Konopacky, Q. M., Macintosh, B., & Barman, T. 2010, Natur, 468, 1080
Matthews, B., Kennedy, G., Sibthorpe, B., et al. 2014, ApJ, 780, 97
Mayor, M., & Queloz, D. 1995, Natur, 378, 355
Metchev, S., Marois, C., & Zuckerman, B. 2009, ApJL, 705, L204
Migaszewski, C. 2015, MNRAS, 453, 1632
Morbidelli, A. 2002, Modern Celestial Mechanics: Aspects of Solar System Dynamics (Boca Raton, FL: CRC Press)
Muterspaugh, M. W., Lane, B. F., Kulkarni, S. R., et al. 2010, AJ, 140, 1657
Papaloizou, J. C. B. 2015, IJAsB, 14, 291
Press, W. H., Teukolsky, S. A., Vetterling, W. T., & Flannery, B. P. 2002, Numerical Recipes in C++: The Art of Scientific Computing (Cambridge: Cambridge Univ. Press)
Price, K., Storn, R. M., & Lampinen, J. A. 2005, Differential Evolution: A Practical Approach to Global Optimization (Berlin: Springer)
Pueyo, L., Soummer, R., Hoffmann, J., et al. 2015, ApJ, 803, 31
Ramos, X. S., Charalambous, C., Benítez-Llambay, P., & Beaugé, C. 2017, A&A, 602, A101
Read, M. J., Wyatt, M. C., Marino, S., & Kennedy, G. M. 2018, MNRAS, 475, 4953
Šidlichovský, M., & Nesvorný, D. 1996, CeMDA, 65, 137
Soummer, R., Brendan, J., Pueyo, L., et al. 2011, ApJ, 741, 55
Ter Braak, C. J. F. 2006, Stat. Comput., 16, 239
Wang, J. J., Graham, J. R., Dawson, R., et al. 2018, AJ, 156, 192
Wertz, O., Absil, O., Gómez González, C. A., et al. 2017, A&A, 598, A83
Wilner, D. J., MacGregor, M. A., Andrews, S. M., et al. 2018, ApJ, 855, 56
Wolszczan, A., & Frail, D. A. 1992, Natur, 355, 145
Yu, Q., & Tremaine, S. 2001, AJ, 121, 1736
Zurlo, A., Vigan, A., Galicher, R., et al. 2016, A&A, 587, A57